Postglacial relative sea level change in Norway

Roger C. Creel [a, *], Jacqueline Austermann [a], Nicole S. Khan [b], William J. D'Andrea [a], Nicholas Balascio [c], Blake Dyer [d], Erica Ashe [e], William Menke [a]

[a] *Lamont-Doherty Earth Observatory, Columbia University, New York, USA*
[b] *Dept of Earth Science and Swire Institute of Marine Science, University of Hong Kong, Hong Kong*
[c] *Department of Geology, College of William and Mary, Virginia, USA*
[d] *School of Earth and Ocean Sciences, University of Victoria, Victoria, Canada*
[e] *Department of Earth and Planetary Sciences and Rutgers Institute of Earth, Ocean, and Atmospheric Sciences, Rutgers University, New Jersey, USA*

ARTICLE INFO

ABSTRACT

We present the first comprehensive postglacial relative sea-level (RSL) database for the Norwegian coast from Oslo to the Kola Peninsula. The database spans the last 20 kyrs and is composed of 413 index points and 610 limiting data points derived from raised beaches, archeological data, glaciomarine terraces, and sedimentary indicators from isolation basins, salt marshes, and peat bogs. The data are quality controlled, assigned standardized indicative meanings, and recalibrated to current standards. We use an ensemble of Bayesian statistical models, trained on sea-level index points and weighted by their fit to both index and sea-level limiting points, to assess the spatiotemporal patterns of Norwegian RSL change. Continuous RSL fall driven by isostatic rebound in response to Eurasian ice sheet collapse dominates the RSL signal at every inland location in Norway. A first transgression (episode of RSL rise), which occurred in southwest Norway during the Younger Dryas (14–11.7 ka), increased RSL by as much as 15 m in some locations. A second transgression, named the Tapes transgression, occurred during the early-mid Holocene between 10 and 5.5 ka. The spatiotemporal model ensemble constrains the timing, amplitude, and spatial distribution of the Younger Dryas and Tapes transgressions. Based on our modeling results, we speculate that the Tapes Transgression was the result of global mean sea level rise temporarily outpacing isostasy-driven RSL fall, while the Younger Dryas Transgression was likely the result of local ice sheet readvance combined with low viscosity asthenosphere and weak lithosphere in the region. We also describe the effects of peripheral bulge migration on Norwegian RSL, which caused increased RSL in the early Holocene and a delayed Tapes transgression. We show that postglacial RSL data in Norway contain complex spatiotemporal patterns of nearfield RSL change that can best be estimated by combining a high-quality data compilation with glacial isostatic adjustment modeling via a robust statistical model.

© 2022 Elsevier Ltd. All rights reserved.

1. Introduction

Global mean sea level (GMSL) was 125–130 m below present during the Last Glacial Maximum (LGM) (Peltier et al., 2015; Austermann et al., 2013) and rose rapidly during the deglaciation as temperatures warmed, ocean circulation patterns changed, and the Northern Hemisphere ice sheets destabilized (Baggenstos et al., 2019; Tierney et al., 2020; McManus et al., 2004). The collapse of the Eurasian ice sheet complex (EIS) likely caused ~12 m (m) of GMSL rise (Hughes et al., 2016; Patton et al., 2017). However, the timing and spatial pattern of EIS melt leading up to its disintegration, particularly in the Barents Sea sector, remain uncertain (Kachuck and Cathles, 2018). For example, melt from the Laurentide, Antarctic, and Eurasian ice sheets drove the fastest period of deglacial GMSL rise, Meltwater Pulse 1a (MWP-1a), which occurred at ~14.6 ka and contributed 15–20 m to GMSL rise, yet the exact amount that each ice sheet contributed remains contested (Stanford et al., 2006; Liu et al., 2016; Lin et al., 2021). Estimates of the EIS contribution to MWP-1a range from 0 to 60% of the total GMSL change associated with the meltwater pulse (Lin et al., 2021; Brendryen et al., 2020). After collapse of the EIS was completed (~9.7 ka), GMSL continued to rise due to the final termination of the Laurentide Ice Sheet (~7 ka, Ullman et al., 2016; Stokes, 2017). GMSL is thought to have stabilized within a few meters of present-day sea

---

level as early as ~6−7 ka (Peltier et al., 2015; Abe-Ouchi et al., 2015) or as late as ~2−4 ka (Bradley et al., 2016; Lambeck et al., 2014). Variations in Greenland, Antarctic, and mountain glacial ice volume since GMSL reached present-day levels have been proposed, though the magnitudes of those changes were likely less than a meter (Young et al., 2020; Kingslake et al., 2018; Greenwood et al., 2018; Davis et al., 2009).

Local RSL change in Fennoscandia is predominantly a result of the combined effects of GMSL rise and glacial isostatic adjustment (GIA), which is the response of the solid earth, its gravity field, and rotation axis to changes in ice and ocean load (Farrell and Clark, 1976; Milne and Mitrovica, 1998). In Northern Europe, EIS disintegration caused land uplift in regions previously covered by the EIS and subsidence in regions near the former ice sheet's edges that had been elevated by displaced mantle material − an effect termed 'peripheral bulge subsidence'. The peripheral bulge likely migrated inland and subsided as the EIS ice margin retreated, as occurred during Laurentide ice sheet collapse (Scott et al., 1987; Barnhardt et al., 1995). RSL change driven by EIS isostatic rebound and peripheral bulge subsidence overwhelmed smaller changes driven by hydro-isostatic loading, continental levering, and ocean siphoning, which govern far-field GIA responses (Mitrovica and Milne, 2002). Isostatic adjustment continues across Fennoscandia today, where uplift rates are documented by GPS, gravity, and tide gauge measurements (Milne et al., 2001; Sjöberg and Bagherbandi, 2020; Vestøl et al., 2019).

Post-LGM RSL change in Northern Europe is highly sensitive to lateral and radial variations in the physical properties of the solid earth, most notably viscosity, as well as to spatiotemporal patterns in ice sheet mass change (Steffen and Kaufmann, 2005; Lambeck et al., 1998; Auriac et al., 2016). Lithospheric thickness varies from <70 km in southern Norway to >120 km beneath the East European craton (Artemieva, 2019). Scandinavian lower mantle viscosity estimates are variable and range from $< 5 \times 10^{21}$ Pa s (Lambeck et al., 1998) to an order of magnitude greater (Steffen and Kaufmann, 2005). Upper mantle viscosities beneath Scandinavia are constrained to $3-5 \times 10^{20}$ Pa s (Steffen and Wu, 2011, and references therein). Local studies of southern Norway, however, have found that sea-level data are better fit with upper mantle viscosities an order of magnitude lower than average values for the rest of Scandinavia (Fjeldskaar and Amantov, 2018). Similar lateral gradients in solid Earth structure alter RSL by meters in West Antarctica (Hay et al., 2017; Nield et al., 2018), and may have done the same in Northern Europe (Fjeldskaar and Bondevik, 2020). For instance, the Younger Dryas (YD, ~14.0−11.7 ka) readvance of the EIS in southwestern Norway — an area thought to have thin lithosphere and weak viscosity structure (Rickers et al., 2013; Schoonman et al., 2017) — coincided with an RSL transgression in southwestern Norway not recorded elsewhere along the Norwegian coast (Mangerud et al., 2016; Fjeldskaar and Amantov, 2018). Similarly, a transgression observed across Fennoscandia, named the Tapes Transgression after the freshwater mollusc *Tapes decussata*, reached its largest amplitude in southwestern Norway (Fjeldskaar and Bondevik, 2020).

In addition to GMSL changes and GIA effects, tectonic deformation has affected RSL around Fennoscandia. Mass unloading during EIS deglaciation caused changing stress regimes in the lithosphere, which led to pulses of seismic activity (Lagerbäck and Sundh, 2008; Olesen et al., 2013). Concentrated in the early Holocene (11−9 ka) but continuing to the present, these episodes complicate the standard depiction of Fennoscandia as a stable continental margin (Faleide et al., 2008). Earthquakes and destabilized gas hydrates along the Norwegian continental margin may also have triggered several submarine mass failures over the last glacial cycle (Mienert et al., 2010; Smith et al., 2013). The most prominent such mass failure, the Storegga Slide, dated to 8.1 ± 0.1 ka (Bondevik et al., 2012; Dawson et al., 2011), spawned a tsunami whose deposits have complicated the interpretation of early Holocene sea-level records along the Norwegian coastline (Bondevik et al., 1997b; Gaffney et al., 2020).

Evidence of GMSL rise, GIA-driven rebound, and smaller scale tectonic events is preserved in Scandinavia's abundant geomorphological archives, which include raised beaches, marine deltas, and more than 400,000 lakes. This sedimentary record extends nearly twenty thousand years into the past and differs dramatically across the region. RSL is recorded in the form of index points that mark the past position of RSL at a given place and time, and limiting points that place an upper or lower bound on past RSL. Scandinavians have measured RSL in Northern Europe for more than 500 years, a legacy that has produced strong constraints on RSL (Celsius, 1743; Ekman, 1991). Recent studies have used preexisting sea-level data to improve EIS reconstructions (Steffen et al., 2013; Steffen and Kaufmann, 2005), bound estimates of lithospheric thickness (Lambeck et al., 1998; Steffen et al., 2014), and confirm models of the lateral heterogeneity of the region's mantle viscosities (Huang et al., 2019). However, existing analyses only use a small subset of Norway's RSL data, many of which were produced in the 1950's or earlier (e.g. Fægri, 1944; Nydal, 1959, and references therein) and have yet to be aggregated into a quality-controlled, standardized database. Small datasets and a lack of data aggregation and standardization make it hard to disentangle and understand the different processes that drive RSL change. Regional sea-level databases, by contrast, can harness the spatiotemporal patterns of GIA to constrain the distinct processes that drove RSL change since the LGM (Khan et al., 2019).

Here, we compile the first quality-controlled RSL database spanning the Norwegian coast. The comprehensive database consists of sea-level index points (SLIPs) and limiting data from 20 ka to present derived from raised beaches, archeological data, glaciomarine terraces, and sedimentary indicators including isolation basins, salt marshes, and peat bogs. To compile the data and estimate their uncertainties, we employ standard procedures agreed upon by the sea-level community (e.g. Hijma et al., 2015; Khan et al., 2019) that include defining each indicator's vertical relationship to sea level, calibrating ages to current standards, and assessing sources of temporal and vertical uncertainty. We employ an spatio-temporal empirical hierarchical model ensemble (STEHME) with Gaussian process regression to calculate spatiotemporal fields of sea-level change. We use the STEHME fields to map the magnitude and timing of the YD and Tapes transgressions and to identify areas where ICE-6G (Peltier et al., 2015; Argus et al., 2014) and GLAC-1D (Abe-Ouchi et al., 2015; Tarasov et al., 2012; Tarasov and Richard Peltier, 2002; Briggs et al., 2014), two deglacial ice sheet reconstructions commonly used in sea-level modeling, misestimate RSL. These findings yield insights into the deglacial sea-level dynamics of the region. We conclude by discussing events that possibly contributed to the sea-level change patterns observed in these data.

2. Sea-level data

We estimate RSL following the standard protocol developed through the International Geological Correlation Project (IGCP) numbers 61, 200, 495, 588, and 639 (Preuss, 1979; Hijma et al., 2015; van de Plassche, 1982; Shennan et al., 2015; Gehrels and Long, 2007; Padgett et al., 2018). Four conditions must be met for a sample to be labeled as a SLIP or limiting point: the sample must have a calendar age, an elevation, an indicative meaning, and a location known or estimated to within 2 km (Shennan et al., 2015). Other attributes, such as tendency, are useful but not required for

sea-level indicators. The RSL that is recorded by each indicator is estimated following Shennan and Horton (2002):

$$RSL_j = E_j - RWL_j \qquad (1)$$

where E_j is the elevation of sample j in relation to present-day mean tidal level (MTL) and RWL_j is its reference water level. The different sources of uncertainty in E_j and RWL_j are assessed separately for each indicator, and all uncertainties are combined in quadrature to derive a total vertical uncertainty for each indicator. Following Shennan et al. (2015), vertical uncertainties are assumed to be normally distributed and independent. The uncertainties included to account for each source of vertical error are described and justified in Table 1.

2.1. Indicative meaning

The indicative meaning defines the vertical relationship between the elevation of a sea-level indicator and sea level. The indicative meaning has two parts: the indicative range (IR), which delimits the 2σ range in elevation that an indicator occupies, and the reference water level (RWL), which represents the indicator's elevation of formation in relation to tidal levels, such as the midpoint between mean higher high water and highest astronomical tide (MHHW—HAT) (Shennan and Horton, 2002). Data whose indicative meanings cannot with confidence be assigned an upper and lower bound may still be determined to have formed in a terrestrial or marine environment and therefore can be classified, respectively, as having formed above or below a tidal datum, e.g. above MHHW (>MHHW) or below MTL (<MTL). The indicators employed in this study, along with their indicative meanings and supporting evidence, are described in detail below and summarized in Table 2.

2.1.1. Isolation basins

Isolation basins comprise the majority (n = 624) of the indicators in the database. Isolation basins form when RSL fall disconnects marine inlets from the ocean and transforms them into first brackish lagoons, then freshwater lakes which, following lake infill and terrestrialization, often become peat bogs (Fægri, 1944; Gabrielsen, 1959). Sediment deposition during the isolation records the event in several ways. A lake's lithological profile changes from marine to freshwater facies, a transition typically accompanied by changes in magnetic susceptibility (Bakke et al., 2005), loss on ignition (Snyder et al., 1997), and bulk organic chemistry (Balascio

et al., 2011). Biostratigraphic indicators, including diatoms (e.g. Thomsen, 1982), pollen (Fægri, 1954; Hyvärinen, 1975; Hafsten and Tallantire, 1978), dinoflagellate cysts (Johnsen, 2017; Lid, 2019), and plant macrofossils (Austad and Erichsen, 1987; Solem and Solem, 1997; Lohne et al., 2007) can also mark the isolation. Lake isolation is measured as the height of the basin's bedrock sill relative to MTL (Long et al., 2011). The isolation basin index point does not depend on the depth of the dated soft-sedimentary isolation contact in the sediment column, but instead on the elevation of the sill that connected the basin with the ocean. Though erosion and human activities can lower sill elevations (see Long et al., 2011, section 2.2 for further discussion), isolation basins with sills underlain by bedrock and undisturbed by humans are generally considered among the most reliable of sedimentary indicators in high-latitude locations.

Lake isolation can be partitioned into four stages: (1) the water in a basin's photic zone becomes fresh; (2) marine incursions into the basin cease; (3) sedimentation shifts from marine minerogenic flux to organic-rich terrestrial deposition; and (4) remaining marine water exits the system (Kjemperud, 1986; Long et al., 2011; Lloyd, 2000). Stage 1 corresponds to an indicative meaning of mean high water spring tide (MHWS), while stage 4 maps to mean low water spring tide (MLWS) (Corner and Haugane, 1993; Corner et al., 1999; Baranskaya et al., 2018). Some rapid Norwegian lake isolations compress these stages into 100—200 years and a few centimeters of sediment (Sørensen, 1979; Anundsen, 1985); other slower isolations smear the stages over thousands of years (Prøsch-Danielsen, 2006; Bird and Klemsdal, 1986). Though sedimentation during lake isolation typically is continuous, RSL transgressions that flood isolated basins with seawater often scour lacustrine sediment, creating depositional hiatuses that make it challenging to date the true flooding event (e.g. Thomsen, 1983; Anundsen and Fjeldskaar, 1983). Lake isolation also depends on tidal range, which can change by orders of magnitude over glacial-interglacial cycles as changing sea level alters continental shelf geometry (e.g. Uehara et al., 2006; Griffiths and Hill, 2015). To account for differences in the isolation stage reported as the true isolation, we assign isolation basin index points the conservative indicative range of MHWS-MLWS, following Baranskaya et al. (2018). The RWL is given by the midpoint between MLWS and MHWS. Because freshwater gyttja is not typically deposited in brackish conditions, the 150 isolation basin terrestrial-limiting points reported here are assigned > MHWS as an indicative meaning. We also recognize marine limiting datapoints from isolation basins (n = 177) where

Table 1
Sources of elevational error and associated uncertainties for Norwegian RSL indicators.

Source of elevational error	Associated elevation uncertainty (2σ)
Indicative range (m)	50% of the indicative range described in Table 2
Indicative range modeling (m)	20% of the maximum difference between modeled tidal datums and the local tidal conditions, as calculated at sites with tide gauges (Khan et al., 2017) — included to account for errors in indicative range assessment.
Paleotide indicative range change (m)	50% of the difference between modern- and modeled paleo-IR.
Sampling (m)	0.01 m (after Shennan, 1986).
Tidal range	50% of the tidal range, applied solely to samples collected offshore below MSL to capture additional uncertainty associated with field assessment of sample elevation relative to MSL.
Reference water level modeling	Uncertainty from RWL calculated through linear interpolation from tidal stations, GPR interpolation from tidal stations, and finite element estimation via FES2014, a global tidal model (see text).
GPS (m)	For studies after 1995 that used GPS, 0.1 m unless specified by authors to be lower.
Map (m)	50% of a contour line for elevations measured on topographic maps. Samples with lat/lons rounded to the nearest minute, or those where locations had to be estimated from diagrams, we assigned an additional 1 m uncertainty.
Benchmark (m)	0.1 m to account for any deviations between individual stratigraphic benchmarks and the Norwegian network of reference benchmarks (e.g. NN1954, NN2000).
Leveling (m)	0.1 m for altitudes measured by high precision surveying; 0.3 for all other altitude measurements where techniques are reported. Following Dyke and Peltier (2000) while acknowledging the high quality of Norwegian leveling practices even when not described, altitudes reported without explanation receive 0.5 m plus an additional 1% of the altitude if < 50 m, or 0.05% of the altitude if > 50 m.

Table 2
Indicative meaning and facies description of SLIPs and limiting data in the Norwegian database.

Sample type	Evidence	Reference water level	Indicative range	Data count
Index points				
Isolation basin	Gyttja, mud, clay, or silt mark the transition between freshwater and marine/brackish sediments, supported by diatoms, macrofossils, or pollen assemblages (Kjemperud, 1981a; Stabell, 1980; Long et al., 2011; Romundset et al., 2018)	(MHWS + MLWS)/2	(MHWS-MLWS)	335
Raised Beach	Sand, gravel, and/or boulder deposits in beach facies. Macrofossil assemblages including shells from *Mytilus edulis*, Hiatella arctica, and other intertidal molluscs (Donner et al., 1977; Helskog, 1978; Møller, 1995; Snyder et al., 1996)	(MLLW + HAT+3)/2	(HAT+3) - MLLW	20
Marine Terrace	Shallow subtidal to intertidal facies bearing intertidal macrofossil assemblages (Andersen, 1968; Sørensen, 1979; Hafsten, 1983; Snyder et al., 1996)	(MHWS + MLWS-2)/2	MHWS-(MLWS-2)	1
Salt Marsh	Microfaunal assemblages in marsh sediments related to tidal datums via transfer function with analogous modern assemblages. (Barnett et al., 2015)	Variable. See (Barnett et al., 2015))	Variable. See (Barnett et al., 2015))	23
Peat Bog	Submerged sediments record marine-freshwater transition. Diatoms, pollen, macrofossil assemblages, and/or geochemical indicators confirm contact (Møller, 1984; Vorren and Moe, 1986)	(MHWS + MLWS)/2	MHWS-MLWS	32
Limiting Data				
Terrestrial limiting	Lacustrine gyttja containing freshwater shell and diatom assemblages that does not warrant index point classification; aeolian, alluvial, lacustrine, or bog sediment; not directly linked to sea level (e.g. Prøsch-Danielsen, 2006)	MHWS	>MHWS	261
Marine limiting	Marine, glaciomarine, or isolation basin sediments containing in-situ marine shells, foraminiferal assemblages, diatoms, or identifiable geochemical signals in clastic sediment (e.g. Balascio et al., 2011)	MTL	<MTL	157

marine macrofossils were dated prior to isolation or following ingression; these datapoints are assigned an indicative meaning of <MTL.

2.1.2. Raised beaches

Raised beaches in Norway are found primarily in Finnmark and along the Varanger peninsula. Composed of sand, gravel, pebbles, and other coarse littoral material, they form when glacioisostasy lifts shorelines above the influence of wave action. Although Norwegian raised beaches were once thought to be precise sea-level indicators (Fletcher et al., 1993), the heterogeneous morphology of northern Norwegian raised beaches complicates their interpretation (Sanjaume and Tolgensbakk, 2009). Local environmental conditions such as prevailing wind direction, wave height, coastal geometry, storm fetch, and extreme wave return period, have been found to control beach structure and indicative meaning (e.g. St-Hilaire-Gravel et al., 2010; Simkins et al., 2015; Kelsey et al., 2015). We therefore assign the 20 raised beach indicators that were well-described when first reported (e.g. Donner et al., 1977; Møller, 1995) an indicative meaning of mean lower low water (MLLW) to 3 m above HAT (cf. Vacchi et al., 2018; Baranskaya et al., 2018). The remaining 17 raised beach observations, whose original descriptions are not sufficient to classify them as SLIPs, are deemed terrestrial limiting points. Their indicative meanings are defined as higher than highest astronomical tide (>HAT).

2.1.3. Archeological/cultural sites

Humans may have migrated north along the Norwegian coastline as early as 10.2 ka (Prøsch-Danielsen, 1993; Glørstad, 2016). Radiocarbon-dated traces of their habitation are frequently used as terrestrial limiting data (e.g. Bang-Andersen, 2003; Prøsch-Danielsen, 2006; Solheim and Persson, 2018; Høgestøl et al., 2019; Helskog, 1978) because uncertainty about the indicative meaning of archeological sites typically limits their utility as index points. We therefore deem all archeological data (n = 183) to be terrestrial-limiting points that formed above MHWS (>MHWS).

2.1.4. Marine terraces

Marine terraces form when isostatic or tectonic uplift elevates shallow marine wave-cut benches, deltaic deposits, glaciomarine outwash, or other sedimentary features. Even before Norwegian

marine terraces and relict shorelines were assigned absolute dates, they were used to identify the prominent sea-level rise events now known as the Tapes and YD transgressions (Tanner, 1906; Fægri, 1944; Gabrielsen, 1959; Marthinussen, 1974). Radiocarbon dates on marine terraces typically come from bivalves including blue mussels (*Mytilus edulis*), European flat oysters (*Ostrea edulis*), and saltwater clams such as the blunt gaper (*Mya truncata*) and wrinkled rock-borer (*Hiatella arctica*). These bivalves, when found unbroken, in growth position, and near the top of a marine terrace formed near past sea level, can serve as sea-level indicators (Andersen, 1968; Grothaug Andersen, 1975). We assign the one such indicator an indicative meaning of 2 m below MLWS to MHWS. Terraces with less supporting evidence, as well as glaciomarine sediment deposits without terrace morphology, are marine-limiting datapoints (n = 44) and assigned an indicative meaning of <MTL.

2.1.5. Sedimentary indicators

Beyond Norway's plentiful isolation basins, tight sedimentary constraints on RSL are derived from salt marshes and peat bogs. The most precise sedimentary indicators come from the Lofoten-Vesterålen archipelago, where geochemical profiles of anthropogenic pollution were combined with radiocarbon dates and visual assessments of foraminiferal assemblages, loss-on-ignition analysis of organic carbon and $CaCO_3$, grain size, and lithostratigraphy to create 23 late-Holocene index points (Barnett et al., 2015). Depending on their stratigraphic position, Barnett et al. (2015) assigned these salt marsh index points indicative meanings ranging from MHHW - HAT to between lowest astronomical tide and mean lower low water tide (LAT - MLLW). Additional indicators are derived from terrestrial peat bogs and peat bogs that sea-level transgression has flooded, termed seashore mires (Vorren and Moe, 1986). The majority of dated peat bog deposits are deemed limiting points with indicative meanings of greater than MHWS (terrestrial) and less than MTL (marine). However, bog deposits that have sufficient accompanying information (n = 32)—e.g. continuous sedimentary successions with radiocarbon-dated transgressive or regressive contacts that overlay incompressible substrates—are interpreted as index points and assigned MLWS-MHWS indicative meaning.

2.2. Age determination

The ages of nearly all index and limiting points included in this database were estimated using radiocarbon (^{14}C) measurements on sediments, macrofossils, bones, marine shells, charcoal, and midden deposits. More than half of the ^{14}C measurements were performed on bulk sediment samples of peat. Bulk sample dates are less precise than dates from macrofossils, shells, or other identifiable material, for two reasons: undifferentiated sediment can (1) inherit older carbon from dissolved limestone or relict organic material (e.g. Hendy and Hall, 2006) and (2) undergo diagenetic alteration from freshwater leaching or acid that contemporaneous roots excrete, which typically skews sediment age young, a phenomenon especially common in oligotrophic lakes (Kaland, 1984). Hu (2010) argues that though the botanical and mechanical effects which skew bulk ^{14}C ages — e.g. root penetration and the reworking of older organic material, respectively — tend to cancel each other out, extra uncertainty to account for the dominant influence of one or the other is prudent. Following suit, we add 100 years of uncertainty to bulk ^{14}C dates to account for this additional noise. Early measurements of ^{14}C were typically not corrected for isotopic fractionation, as modern laboratories do (Stuiver and Polach, 1977). All samples in this database that were dated before 1975 were measured at the radiocarbon laboratories at the universities of Trondheim (T-), Helsinki (Hel-), or Lund (Lu-), which began reporting isotope-corrected ^{14}C starting respectively in 1978, 1983, and 1962 (Håkansson, 1969; Gulliksen et al., 1978; Jungner and Sonninen, 1989). Samples older than these dates from each institute were corrected and assigned additional uncertainties following Törnqvist et al. (2015).

All ^{14}C ages from terrestrial sources were calibrated to calendar years using Intcal20 (Reimer et al., 2020). Dated marine samples younger than 12.2 ka were calibrated with Marine20 and assigned a local reservoir correction ΔR and uncertainty based on a weighted mean of nearby corrections from the CALIB Marine Reservoir Correction Database (http://calib.qub.ac.uk/marine/; Heaton et al., 2020). ΔR values varied from −224 ± 80 to 21 ± 239 yrs, with a mean of −150 ± 58 yrs. Marine ^{14}C ages older than 12.2 ka were calibrated using NorMarine18, a calibration curve derived from Norwegian sea sediment cores that accounts for the older age of Norwegian seawater carbon during the deglacial, and were not assigned an additional local reservoir correction (Brendryen et al., 2020). The NorMarine18 calibration curve assumes a marine reservoir age slightly older than Marine20 (<0.1 ka) between 12.2 ka and 14.6 ka, and much older (~ 0.8−1.5 ka) between 14.6 and 19 ka. Positive and negative 2σ uncertainties, calculated in quadrature from errors in measurement, isotopic fractionation, reservoir correction, and bulk analysis, were assigned to each age. Ages were rounded to the nearest decade and reported in thousands of years before 1950 CE (ka, Stuiver and Polach, 1977). Calibrations were performed with the Iosacal Python library (Costa, 2018).

Several isolation basin index point ages in the database were originally calibrated using Bayesian calibration software tools that combine knowledge from many ages at a single site into a single calendar year estimate (e.g. Romundset et al., 2018; Rasmussen et al., 2018; Romundset et al., 2011, 2010a,b). Only isolation basin SLIPs were originally calibrated in this way. Eight late-Holocene index points from the Lofoten-Vesterålen peninsula were dated using ^{210}Pb, ^{137}Cs, and ^{241}Am, details of which are described in Barnett et al. (2015). To increase the utility of the database, we report all radiocarbon dates, calibrate each age individually, and label the associated indicators as either limiting or index points based on their stratigraphic context. In nearly all cases, this choice increases age uncertainties but does not appreciably change the estimate of the basin's mean calendar age of isolation.

2.3. Estimating uncertainties in RSL

Modern tidal datums related to indicative meanings were estimated by a composite method. First, tidal datums were gathered from all Norwegian tide gauges (n = 15) maintained by the Norwegian Mapping Authority (2021). Relevant tidal datums for each data location were estimated using a distance-weighted average of the two tide gauges closest to each datum. Second, the tidal datums were combined via Gaussian process regression (GPR) with a Matérn 5/2 kernel to produce a smooth spatial field that was sampled at the location of each RSL observation (Rasmussen and Williams, 2006). Third, each tidal datum was calculated using FES2014, a global tidal model with enhanced accuracy in arctic regions (Carrere et al., 2015). The distance-weighted prediction, GPR prediction, and tidal model were combined to produce a mean and standard deviation for each tidal datum, which was included as a spatially-varying reference water level modeling uncertainty.

Many factors controlling tidal ranges along Norway's > 100,000 km coastline, including local bathymetry, tidal dissipation, and the resonance structure of the oceans, were substantially different before GMSL neared present-levels in the mid-Holocene (Thomas and Sündermann, 1999). It is therefore important to consider paleotidal range changes for sea-level indicators older than ~6 ka. Paleotidal reconstructions, however, typically depend on estimates of paleobathymetry derived from GIA models. Because GIA models themselves are calibrated on sea-level indicators whose indicative meanings may come from paleotidal reconstructions, it is challenging to create a paleotidal modeling framework independent from the choice of GIA-modeled sea level that drives it. Independent constraints that can groundtruth deglacial paleotidal range estimates are also rare (Griffiths and Peltier, 2009). It is therefore common practice to include paleotidal range changes by increasing SLIP uncertainties rather than using a paleotidal correction itself (e.g. Khan et al., 2017). We follow this practice by adding uncertainty to all index points based on the difference between modern datums (calculation described above) and datums from a 2D paleotidal model of Northwestern Europe based on the Princeton Oceanographic Model, full details of which are found in Uehara et al. (2006).

2.4. Data projection: the isobase method

Norwegian RSL studies typically use empirical maps of constant uplift based on Holocene sea-level data and present-day uplift rates to project nearby data into a single time series — a technique called the isobase method (De Geer, 1888; Hafsten, 1960). The isobase method makes it possible to build complete timeseries out of isolation-basin index points measured at lakes tens of kilometers apart. It is therefore useful in a nearfield region like Norway where uplift histories vary substantially around the coastline. Isobase maps can be inaccurate or misleading, however, because the technique does not include calculation of projection uncertainty, often relies on undated shorelines, and is designed for lines of equal uplift that are straight — such as occur on Norway's west coast — but not curving, such as occur in southern Norway (Romundset et al., 2018).

Nevertheless, the isobase method of projection is an effective tool for grouping sea-level data on a regional level to visualize the spatial heterogeneity of sea-level change close to former ice sheets. We therefore introduce a modified isobase approach. Data are grouped into clusters that follow current regional isobases, have similar STEHME-modeled sea-level histories (see next section), and have data density high enough ($n \geq 5$) to warrant visualization (Hafsten, 1983; Anundsen, 1985; Corner et al., 1999; Lohne, 2006; Romundset et al., 2015; Fjeldskaar and Amantov, 2018). The average

location of each cluster − computed by averaging the latitudes and longitudes of all data in a cluster − is chosen as the plotting site. For each datapoint that is not located at the plotting site, we calculate the difference between the mean STEHME-predicted RSL at the plotting site and the mean STEHME-predicted RSL at the data site; this difference is used as a correction that, for plotting purposes only, is applied to all data from the data site.

3. Bayesian empirical hierarchical model

Space-time correlations in the processes that affect RSL can be leveraged in statistical models to account for known uncertainties, balance the effects of geographic and temporal clustering, fill in gaps in space and time, and integrate disparate observations into a common framework. To that end, we model Norwegian RSL with a STEHME (Ashe et al., 2019). Each spatiotemporal empirical hierarchical model (STEHM) member of the ensemble treats every SLIP as a noisy record of 'true' sea level at a specific point in space-time, and models uncertainty on this 'data level' as uncertainty in the measurement of each indicator's age and height. Prior knowledge about the processes that changed sea level is included via covariance functions that specify how RSL observed in one place influences unobserved sea level modeled elsewhere. Uncertainty on this 'process level' represents uncertainty about the scientific assumptions made in modeling the spatiotemporal RSL field. The hyperparameters used to specify the temporal and spatial length scales over which the processes that formed the true RSL field are correlated, and the amplitude of those processes, are included in a third 'hyperparameter' level, which specifies the prior distribution of each hyperparameter. Each single STEHM produces a point estimate of the maximum likelihood hyperparameter values. Employing a STEHME enables an empirical distribution over hyperparameters to be calculated.

3.1. Data level

Consider the elevation of true RSL $k \in k_1, ..., k_n$ at times $t \in t_1, ..., t_n$ and lat/lon locations $\mathbf{x} \in \mathbf{x}_1, ..., \mathbf{x}_n$. This RSL results from several processes $f \in f_1, ..., f_m$, where each process can be represented through hyperparameters $\theta \in \theta_1, ..., \theta_p$ that characterize its behaviour, and is distributed according to a probability distribution $p(k|\theta)$. Each observation n of that true RSL is noisy in elevation and time:

$$y_n = f_n(\mathbf{x}_n, t_n) + \epsilon_n^y \tag{2}$$

$$T_n = t_n + \epsilon_n^t \tag{3}$$

where ϵ_n^t and ϵ_n^y are assumed to be independent, normally-distributed errors in age and RSL, respectively; y_n is noisy RSL; and T_n is the noisy age of the indicator. Time uncertainties are approximated via the noisy-input Gaussian process method (Mchutchon and Rasmussen, 2011), where age uncertainties are translated via a first-order Taylor-series approximation into equivalent RSL uncertainties (cf. Kopp et al., 2016; Lambeck et al., 1998; Steffen et al., 2013).

3.2. Process level

Sea level is modeled as a spatiotemporal field $s(\mathbf{x}, t)$ with three components:

$$s(\mathbf{x}, t) = h(\mathbf{x}, t) + r(\mathbf{x}, t) + e(t) \tag{4}$$

representing the prior distribution on RSL h, which operates at hemispheric scale; the spatiotemporal process operating at regional scale r; and a temporal field representing white noise $e \sim \mathcal{N}(0, K(t, t'))$, where ~ reads 'is distributed as', $\mathcal{N}$ denotes a normal distribution, and $K(t, t')$ refers to a stationary covariance function (Cressie and Wikle, 2015).

Gaussian processes are completely described by their mean and covariance functions, which define prior expectations about the mean values of the component terms through space and time, the variance of each point, and the correlation among points. The regional and white noise processes are each modeled as a Gaussian process (GP), which is a continuous distribution over stochastic functions, any finite sampling of which is a multivariate normal distribution (Rasmussen and Williams, 2006). The regional process $r(\mathbf{x}, t)$ has a GP prior distribution with zero mean and Matérn covariance functions:

$$r(\mathbf{x}, t) \sim \mathcal{GP}\Big(0, \sigma_r^2 \; \rho(\mathbf{x}, \mathbf{x}'; \; l_r) \; \rho(t, t'; \tau_r)\Big) \tag{5}$$

where σ^2 refers to amplitude, covariance between sample locations $\mathbf{x}$ and $\mathbf{x}'$ at times t and t' is represented by a once-differentiable Matérn covariance function ρ with smoothness parameter 3/2, and l_r and τ_r are, respectively, the geographic and temporal length scale hyperparameters for regional variability (Ashe et al., 2019; Khan et al., 2017).

The hemispheric prior distribution $h(\mathbf{x}, t)$ is represented by the spatiotemporal RSL fields of GIA predictions from two ice thickness histories paired with nine different viscosity models: ICE-6G and its viscosity profile, VM5 (Peltier et al., 2015; Roy and Peltier, 2017; Argus et al., 2014) with a 90 km thick lithosphere; and GLAC-1D (Abe-Ouchi et al., 2015; Tarasov et al., 2012; Tarasov and Richard Peltier, 2002; Briggs et al., 2014) with all possible combinations of an upper mantle viscosity of 3 and 4×10^{20} Pa s, lower mantle viscosity of 1.5 and 3×10^{21} Pa s, and lithospheric thickness of 71 and 96 km. These parameters are consistent with previous GIA-related investigations of Fennoscandian solid earth structures (Lambeck et al., 2006, 2010). The GLAC-1D and ICE-6G ice histories are chosen as priors because of their contrasting postglacial ice distributions, open availability, and widespread use in the sea-level community. A global glaciation phase between MIS-5a (80ka) and LGM is constructed for each model that follows the GMSL curve estimated by Waelbroeck et al. (2002), which is based on RSL data and $\delta^{18}O$ records. Ice geometries for ICE-6G and the GLAC-1D EIS during this interval exactly match post-LGM configurations with the same GMSL value. Pre-LGM geometries for the GLAC-1D Laurentide, Greenland, and Antarctic ice sheets follow published sources (Tarasov and Richard Peltier, 2002; Tarasov et al., 2012; Briggs et al., 2014; Abe-Ouchi et al., 2015). We adopt the density structure and elastic parameters of the Preliminary Reference Earth Model (PREM, Dziewonski and Anderson, 1981).

To calculate RSL associated with these ice histories and viscosity structures, we use the gravitationally self-consistent sea-level model described in Kendall et al. (2005), which simulates the RSL change produced by the gravitational and viscoelastic effects of water and ice mass loading, shoreline migration, and load-driven changes to Earth's rotation axis (Milne and Mitrovica, 1998). First a single GIA-predicted prior spatiotemporal RSL field is subtracted from each RSL index point; then the Gaussian process is fitted to this RSL-GIA difference; then the GIA field is added back to the posterior. This procedure eases computation by improving covariance matrix conditioning and mandating that at locations or times too distant from observations to be influenced by them, modeled sea level reverts to the GIA-modeled prior.

The empirical Bayesian approach, which produces each STEHM

of the STEHME, approximates process hyperparameter distributions with point estimates (l_r, τ_r). The process hyperparameters are optimized by maximizing the log marginal likelihood of their fit to the noisy sea-level data, which for normally distributed observations − as all SLIPs in this study are assumed to be − resembles a root mean squared error (RMSE) metric. After an initial guess, STEHM hyperparameters are optimized using a two-phase global optimizer to find hyperparameter point estimates that produce sea-level fields that best fit the sea-level observations given the chosen covariance functions. The optimizer used is the Scipy basinhopping function (Virtanen et al., 2020), which combines local gradient-descent optimization following the quasi-Newton method of Broyden, Fletcher, Goldfarb, and Shanno (BFGS) (Fletcher et al., 1993) with a global stepping algorithm that mimics energy minimization of atom clusters (Olson et al., 2012). The product is a posterior probability distribution that estimates the 'true' sea-level field $s(\mathbf{x}, t)$ conditional on the optimized hyperparameters.

Relative to fully Bayesian methods that include hyperparameter uncertainties, empirical Bayesian methods underestimate the full uncertainties of predicted RSL (cf. Piecuch et al., 2017). We address the empirical Bayesian limitation by initializing STEHM optimization with 1012 different hyperparameter combinations for each of the 9 GIA-predicted prior RSL estimates. This procedure results in 9108 different reconstructions of the spatiotemporal sea-level field, each of which has a mean and 95% credible interval. Characteristic length and time scales are initialized between 100 and 13000 km and 0.1−10 kyr, hyperparameter ranges that span the temporal and spatial dimensions of the modeled region. We do not bound hyperparameter optimization because sensitivity tests showed that such bounds hinder optimization and decrease model performance. The posterior distribution of hyperparameters, conditioned on the SLIPs, shows most likely spatial length scales on the order of 2500 km and time scales on the order of 2−4 kyr (Fig. 1).

Once optimized to fit the SLIPs, each of the 9108 ensemble members is assigned a posterior likelihood based on its fit to both SLIPs and limiting points. Limiting data probability distributions, which combine each datum's normally-distributed measurement uncertainty and stepwise indicative meaning, are approximated as error functions:

$$p(y_n \mid RSL_{nm}) = \frac{1}{2} + \frac{1}{2} erf\left(c_n \frac{y_n - RSL_{nm}}{\varepsilon_n^y}\right) \tag{6}$$

where $c_n = 1$ when the datum is terrestrial-limiting and $c_n = -1$ when it is marine-limiting, and RSL_{nm} is the STEHME posterior mean m sampled at the age and location of data point n. The associated error e_{nm}, necessary for misfit calculations, is calculated by taking the natural log of $p(y_n \mid RSL_{nm})$ (Menke, 2018, equation 9.6):

$$e_{nm} = -2 \ln\left(\frac{1}{2} + \frac{1}{2} erf\left(c \frac{y_n - RSL_{nm}}{\varepsilon_n^y}\right)\right) \tag{7}$$

Following Auriac et al. (2016), limiting point elevation and age uncertainties are combined with index points and their associated uncertainties via a weighted residual sum of squares (WRSS) calculation to derive fitness scores for each model:

$$WRSS_{nm} = \begin{cases} \left(\frac{2r_{nm}^t}{\epsilon_n^t}\right)^2 + \left(\frac{2r_{nm}^y}{\epsilon_n^y}\right)^2 & c_n = 0 \\ \\ \left(\frac{2r_{nm}^t}{\epsilon_n^t}\right)^2 + e_{nm} & c_n \neq 0 \end{cases} \tag{8}$$

where $c_n = 0$ when a datum n is an index point, r_{nm}^t is the residual in time, and r_{nm}^y is the residual in elevation. To calculate the residual, we find the age of the mean posterior sea level m at data location n that minimizes the distance (in elevation—age space) between the means of the SLIP and the STEHME. We then calculate the residual as the difference between the time and elevation of the modeled sea level at that age, and the time and elevation of the SLIP. $WRSS_{nm}$ values are summed over all data points n to obtain a chi-squared value, χ_m^2, which describes the overall model-data misfit for a given model m:

$$\chi_m^2 = \frac{\sum_{n=1}^{N} WRSS_{nm}}{\sum_{m=1}^{M}\left(\sum_{n=1}^{N} WRSS_{nm}\right)} \tag{9}$$

where N is the number of data and M is the number of different sea-level reconstructions in the GIA prior model ensemble. Note that
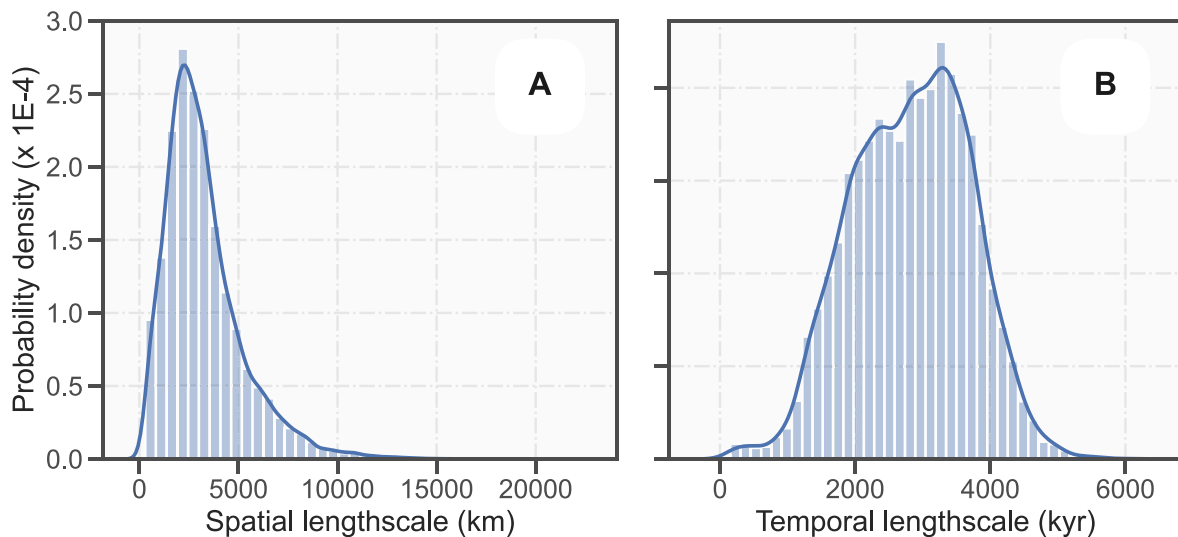

Fig. 1. Posterior distributions of optimized (A) spatial and (B) temporal length scales for Matérn 3/2 covariance kernels used to model the regional to local process in the Bayesian empirical hierarchical model ensemble.

the denominator serves to normalize the weights so that they add up to 1.

A weighted mean of model posteriors $\hat{RSL}_w$ is then computed by multiplying the mean of each posterior reconstruction RSL_m by its χ_m^2 value:

$$\hat{RSL}_w = \sum_{m=1}^{M} RSL_m \cdot \chi_m^2 \tag{10}$$

The total variance of $\hat{RSL}_w$ is calculated as $\hat{RSL}_w$'s weighted mean variance and variance of means, summed:

$$\sigma_{RSL_w}^2 = \sum_{m=1}^{M} \sigma_m^2 \cdot \chi_m^2 + \sum_{m=1}^{M} \chi_m^2 (RSL_m - \hat{RSL})^2 \tag{11}$$

where σ_m^2 is the variance of a given posterior sea-level reconstruction and $\hat{RSL}$ is the unweighted mean of the posterior sea-level reconstruction. The posterior RSL distribution represents the underlying RSL field conditional on the distribution of process hyperparameters (Fig. 1). The uncertainty of $\hat{RSL}_w$ may be larger than a single observation's uncertainty because it accounts for hyperparameter uncertainty. The spatiotemporal continuity of the posterior model allows us to estimate RSL for places and times without data, the uncertainty of which increases with distance from the data. Though single STEHMs are commonly applied to post-glacial sea-level data (e.g. Vacchi et al., 2018; Khan et al., 2017; García-Artola et al., 2018), the procedure outlined above is, to our knowledge, the first instance of an ensemble of STEHMs (i.e. STEHME) applied to postglacial sea-level data. All STEHME calculations presented here are produced using GPflow, a Tensorflow-based GP library in Python (Matthews et al., 2016).

4. Results

The Norwegian database spans the coast of continental Norway from the Kola peninsula in the Barents Sea to the northeastern shores of the North Sea (Fig. 2), in latitude from 58° to 73°N and longitude from 2° to 43°E. The compilation excludes Svalbard. It includes data from more than 100,000 km of Norwegian coastline between 19.4 ka and the present.

The new database is composed of 1023 data points, of which 413 are SLIPs, 433 are terrestrial limiting points, and 177 are marine limiting points. RSL observations cluster in the south: 70% of all data were collected in the southern half of Norway. A majority of the data date to the early Holocene: 76% of index points, 79% of terrestrial limiting data, and 89% of marine limiting data formed before 7 ka. A similar distribution describes data in other areas such as in Arctic Russia, northern Canada, and the Baltic, where rapid early Holocene isostatic uplift preserved more sea-level indicators than slower uplift in the late Holocene (Baranskaya et al., 2018; Vacchi et al., 2018; Rosentau et al., 2021).

Ages and elevations of samples in the database are reported with 2σ uncertainties. For visual convenience, we plot and discuss the corrected elevation of each RSL observation as calculated via the modified isobase approach (see Section 2.4). RSL observations are gathered along lines of similar uplift to minimize correction. As a result, the elevation of index points plotted and referred to in the text will differ to some degree from the raw elevations that can be found in the supplementary materials. In the following we describe the evolution of RSL around Norway starting from the north.

4.1. Russian Kola Peninsula, site 1

The data from the Kola Peninsula (site 1, Fig. 3) include 9 marine limiting points, 1 terrestrial limiting point, and 2 index points.

Derived from emerged shorelines and stratigraphic relations, these data, which accord with isolation basin records already compiled in the region (Baranskaya et al., 2018), describe an RSL stillstand during the early Holocene, then RSL fall to present. Though the highest basins to isolate in the region are located near ~60 m above present sea level (Koshechkin, 1975; Snyder et al., 1997), the data compiled here suggest that RSL on the Murman coast reached 12 ± 2.2 m at 6.2 ka, remained essentially constant until 4.3 ka, and was less than 2.5 m at 1 ka (Snyder et al., 1996). The STEHME aligns with the early Holocene RSL plateau, accords with both index points, and suggests that the Holocene RSL plateau began around 8 ka.

4.2. Varanger Peninsula, sites 2-3

The Varanger Peninsula hosts 14 SLIPs (sites 2 & 3, Fig. 3) from beach ridges (n = 12) and isolation basins (n = 2), as well as 2 marine-limiting data from marine terraces and 54 terrestrial-
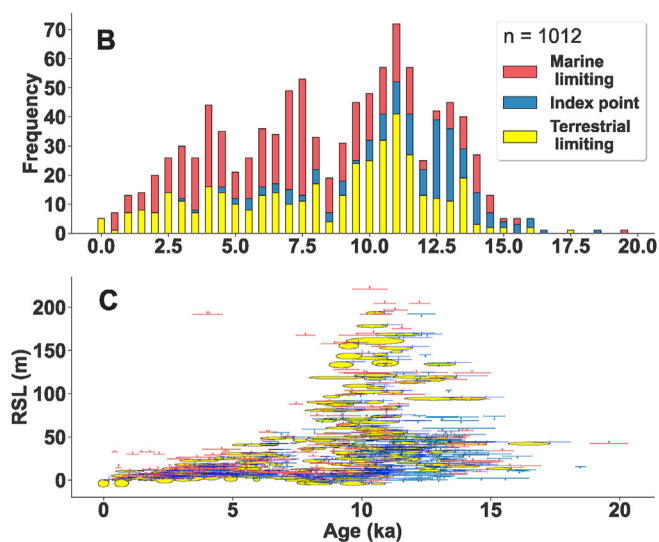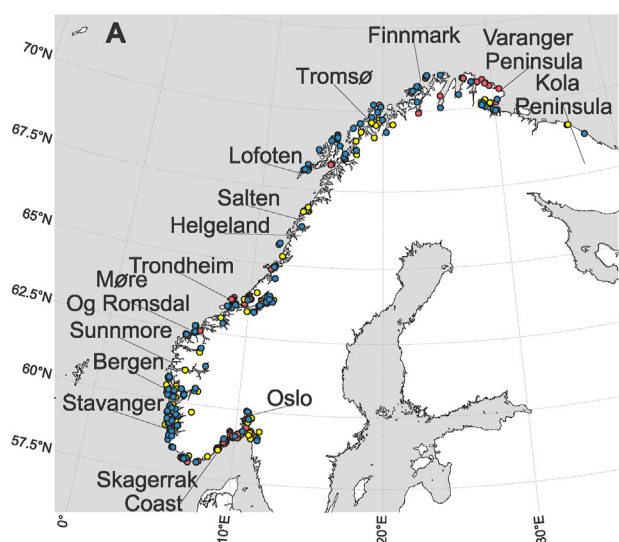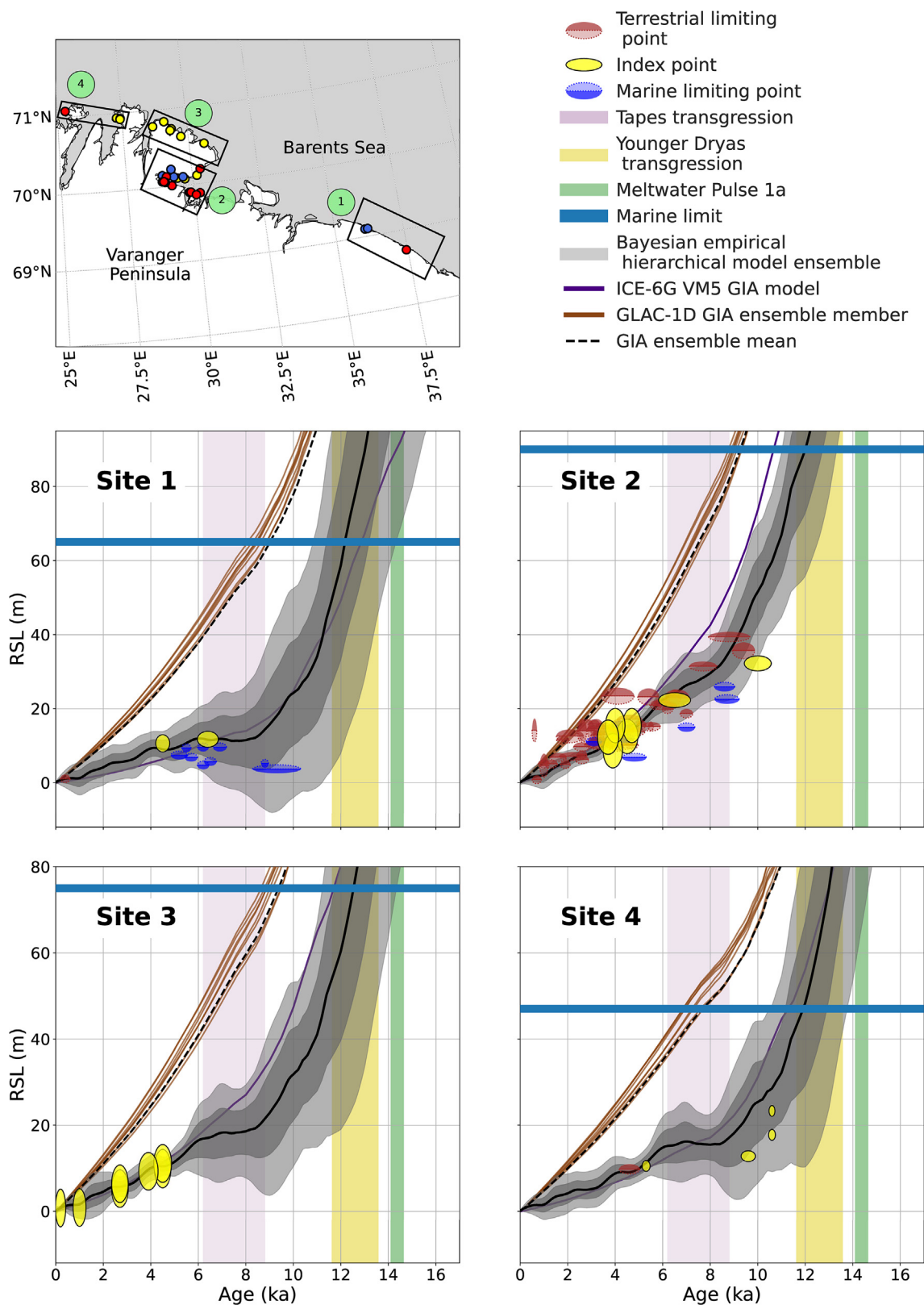

Fig. 2. Distribution of Norwegian RSL data. (A) Spatial distribution of index, marine-, and terrestrial-limiting data (see panel B for legend). (B) Temporal Frequency of Norwegian RSL data. (C) Age and inferred RSL from all locations, plotted by indicator type. All ages and RSL estimates are reported with 2σ uncertainties.

Fig. 3. RSL data, data distribution, and spatiotemporal statistical model predictions for north Norway: (1) Kola Peninsula, (2) South Varanger peninsula, (3) North Varanger peninsula, (4) Nordkinn. Data on map are shown as markers that are color coded by indicator type. Age and vertical uncertainties for indicators in timeseries plots are reported as 2σ. The statistical posterior model (STEHME) is shown in grey; the light grey band is the 95% credible interval, the dark grey band is the 68% credible interval, and the mean is shown as a black line. The ensemble of GIA prior models, consisting of predictions from ICE-6G VM5 and GLAC-1D with a range of solid earth structures, is shown as brown (GLAC-1D), purple (ICE-6G), and dotted black (GIA ensemble mean) lines. Vertical bands denote notable time intervals, including Meltwater Pulse 1a, the Younger Dryas transgression, and the Tapes transgression. The marine limit line describes the highest marine sediments measured at each site or modeled from available constraints (cf. http://geo.ngu.no/kart/losmasse_mobil/). (For interpretation of the references to color in this figure legend, the reader is referred to the Web version of this article.)

limiting beach ridge, sedimentary, and archeological data (Helskog, 1978; Donner et al., 1977; Schanche, 1988; Møller, 1987). The data describe a continuous sea-level fall over at least the last ten thousand years, with the falling RSL remaining consistent at ~2 cm/yr throughout the Holocene. While the majority of archeological data cluster between 10 and 20 m and 4–5 ka, sedimentary indicators extend from 32.2 ± 2.0 m at 10.0 ka to 0.9 ± 1.1 at 0.6 ka. The preponderance of mid-Holocene limiting points and single early-Holocene index point at 10.0 ka accord with the STEHME.

4.3. Finnmark, sites 4-7

The RSL history of Finnmark (sites 4–7, Fig. 3 4) is derived from isolation basin index points (n = 17), terrestrial-limiting points from peat bogs (n = 7) and isolation basins (n = 5), and marine limiting points from cobble shores (n = 2), peat bogs (n = 2), isolation basins (n = 3), and marine terraces (n = 2) (Marthinussen, 1962; Nydal, 1960; Donner et al., 1977; Gulliksen et al., 1978; Andersen, 1968; Rickerich, 2018; Kui, 1996; Fodnes, 1996). RSL index points at coastal locations in Finnmark, all below ~25 m, first occur at 10.6 ka. When combined with a marine limit higher than 50 m, this implies 25 m of largely-unrecorded post-glacial RSL fall. After 10.6 ka, a slight transgression occurred between ~8 ka and ~5.5 ka − hereafter termed the Tapes transgression − though the magnitudes of regression and transgression vary among sites. At Nordkinn (site 4), data suggest that the early Holocene lowstand of ~13 m was reached by 9.6 ka, after which RSL transgressed a small amount before falling again after 5 ka. The STEHME captures the Tapes transgression pattern in this region and, despite the few index points in Finnmark, fits the data within uncertainties.

At Rolvsøya (site 5), seven isolation basin index points constrain sea level to have reached 5.8 ± 1.2 m by 11.2 ka and remained no more than a meter higher than that level until 5.1 ka, when it fell until the present. Similarly, at Sørøya (site 6), isolation basins (Romundset et al., 2018) and driftwood from raised beaches (Marthinussen, 1960) constrain sea level to have reached 17 ± 1.3 m by 11.1 ka, continued falling to 11.0 m ~8.1 ka, then remained constant for 1.7 kyr. After 6.2 ka, sea level likely regressed to the present shoreline. At both sites, the STEHME captures a mid-Holocene transgression and the isolation basin index points before 10 ka, though few, are still sufficient to lower the early Holocene STEHME mean enough to fit the data.

RSL records further inland (site 7) do not preserve the transgression recorded on the coast. Instead, the inland record, consisting of three isolation basin index points and eight limiting points, two marine-limiting marine terraces, and three terrestrial-limiting peat bogs, is consistent with a pattern of rapid deglacial and slower Holocene RSL fall also present on the Varanger Peninsula (Kui, 1996; Fodnes, 1996; Gulliksen et al., 1978; Donner et al., 1977; Andersen, 1968; Marthinussen, 1962; Nydal, 1960). The STEHME is consistent with all indicator points at this site.

4.4. Troms, sites 8-9

The record from Troms consists of 15 index points and three limiting points from isolation basins, 11 marine limiting points from marine terraces, and 11 terrestrial limiting points from raised beaches (sites 8 & 9, Fig. 6). Inland (site 8), the early Holocene record is derived from marine terraces, the highest of which constrain sea level to more than 71.7 ± 1.3 m by 13.8 ka (Andersen, 1968; Nydal, 1959, 1960; Bakke et al., 2005). Sea-level data then record sea level falling by as much as 45 m after 13.3 ka, reaching a still-stand or small transgression between 9.6 ka and 6.8 ka, before falling to present-day sea level (Corner and Haugane, 1993; Rasmussen et al., 2018). The STEHME reproduces the transgression

described by Corner and Haugane (1993), and in the early Holocene to is consistent within uncertainties with the isolation basin index points.

Towards the coast (site 9), the mid-Holocene Tapes Transgression is constrained by beach ridges (Møller, 1984, 1987, 1995; Nydal et al., 1970; Hald and Vorren, 1983) and isolation basins (Corner and Haugane, 1993) to not more than 9.5 m by 6.6 ka before RSL falls to the present-day shoreline. Though only two isolation basin data constrain the site 9 curve, nearby index points shape the STEHME mid-Holocene transgression (site 11) and enforce low sea level in the late Holocene (site 10), consistent with both a deglacial (13.5 ka) index point at 52.7 ± 1.9 and a late Holocene index point at 7.9 ± 1.7 m (site 9).

4.5. Nordland, sites 10-11

The RSL record from Nordland contains 43 index points from isolation basins, salt marshes, and peat bogs; 21 marine-limiting points from marine terraces and isolation basins; and 45 terrestrial-limiting points from raised beaches, isolation basins, and archeological sites (sites 10−11, Fig. 5). In the inland of the Vesterålen archipelago (site 10), marine terrace (n = 7) and beach ridge (n = 2) limiting data indicate that RSL was ~70.8 m at 15.1 ka, then fell rapidly until the mid-Holocene, when the rate of regression slowed (Lid, 2019; Billah, 2020; Møller, 1987; Andersen, 1968; Nydal et al., 1964; Marthinussen, 1962; Nydal, 1962). Salt marsh index points from Hinnøya, in south Vesterålen, tightly constrain RSL since 3.3 ka to less than 2 m (Barnett et al., 2015). The STEHME describes a slight RSL transgression in the early Holocene and an RSL plateau in the late Holocene. It agrees with the isolation basin data within uncertainties.

In Lofoten and northwest Vesterålen (site 11), limiting data from raised beaches, peat bogs, archeological sites, a marine terrace, and three isolation basins constrain RSL to have fallen >60 m from an elevation greater than 45.8 ± 1.1 m at 3 ka to below present-day RSL in the earliest Holocene (Marthinussen, 1962; Vorren et al., 1988; Midtun, 2019; Møller, 1984, 1986; Nydal et al., 1964; Vorren, 1978; Vorren and Moe, 1986; Balascio et al., 2011; Vetti, 2020). After reaching a YD lowstand, RSL then transgressed to 6.5 ± 1.3 m at 5.1 ka before falling to the present.

Lofoten and Vesterålen index points produce a pronounced mid-Holocene transgression in the STEHME, and abundant index point constraints after 10 ka (site 11) enforce that the STEHME mean passes up to 20 m below present-day MTL at 16 ka, contrary to several marine limiting points and one index point between 12 and 17 ka, though all data fall within the STEHME's uncertainty. This tradeoff is reflected in large uncertainties at site 11 prior to 10 ka.

4.6. Svartisen, salten, and helgeland, sites 12-13

The sea-level histories of Svartisen, Salten, and Helgeland (sites 12 & 13, Fig. 5) are delimited by isolation basin index points (n = 7), marine-limiting marine terraces (n = 9), and terrestrial-limiting isolation basin data (n = 4) (Ramfjord, 1982; Nydal, 1960; Nydal et al., 1972; Rasmussen, 1981; Møller, 1986). In Svartigen (site 12), 7 marine-limiting sedimentary indicators constrain RSL to have been higher than 40.0 ± 1.3 m at 9.8 ka (Rasmussen, 1981). Though no index points exist in this region, the STEHME is consistent with all marine limiting points. In Salten and Helgeland, further to the south (site 13), RSL fell rapidly from 128.3 ± 1.9 m at 11.4 ka to 54.9 ± 1.9 m at 7.9 ka (Ramfjord, 1982; Nydal et al., 1972; Nydal, 1960). Uniform regression continued through the Holocene at a slower rate.
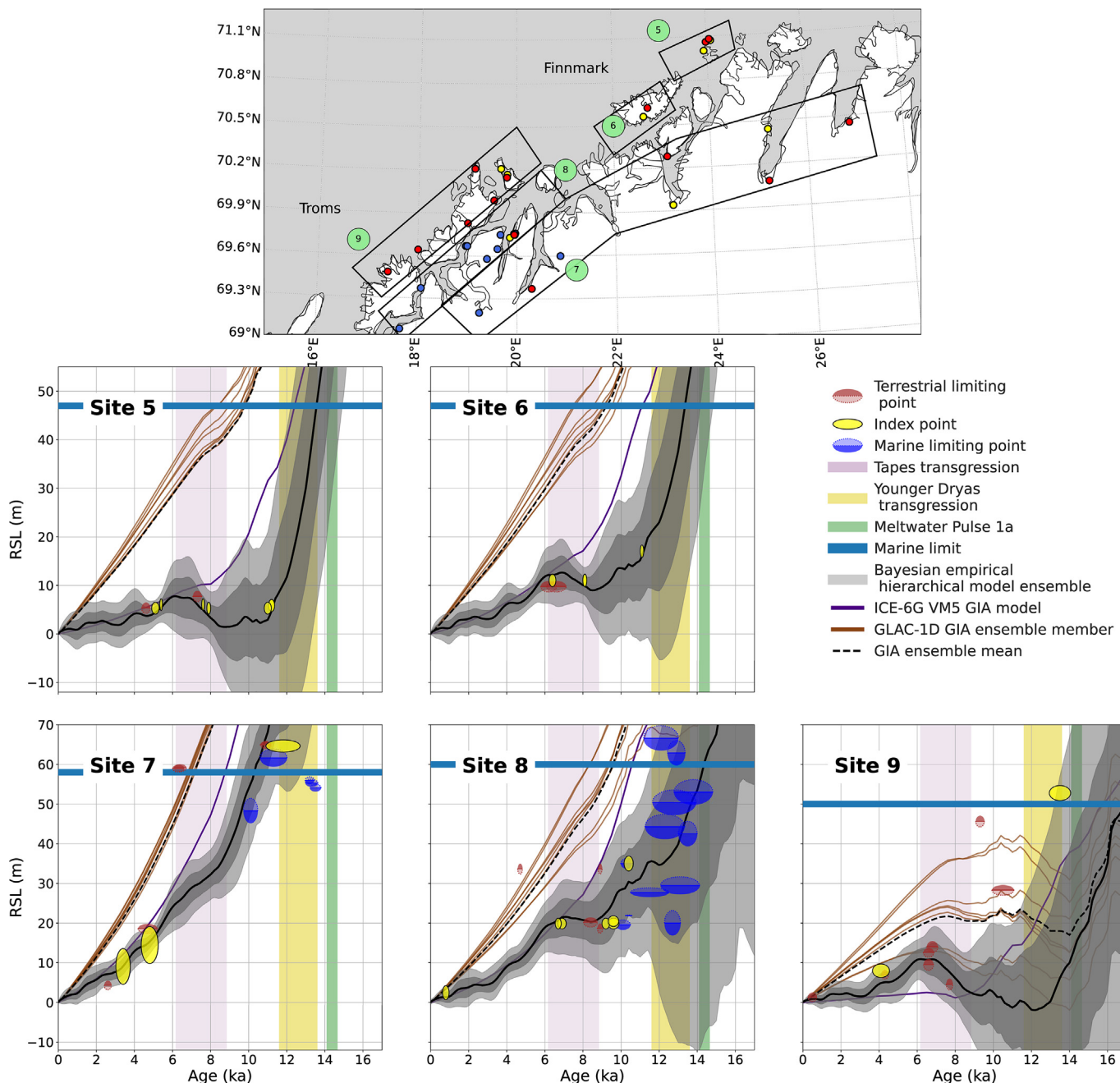
Fig. 4. Same as Fig. 3 but for northwest Norway: (5) Rolvsøya, (6) Sørøya, (7) Inland Finnmark, (8) Inland Troms, (9) Coastal Troms. See Fig. 3 caption for details.

4.7. Trondheimsfjord, sites 14-15

The RSL record from east Trondheimsfjord (site 14, Fig. 6) in-cludes 17 isolation basin index points, 12 terrestrial limiting data from isolation basins and raised beaches, and 7 marine-limiting data from marine terraces (Sveian and Olsen, 1984; Kjemperud, 1981a,b, 1986; Gulliksen et al., 1978; Nydal et al., 1972, 1970). RSL fell from 170 ± 1.8 m at 12.3 ka to 47.7 ± 1.5 m at 6.8 ka, then continued falling at a slower rate (~0.6 cm/yr) until the present. As at site 13, the STEHME maps a fast rate of RSL fall between 12 and 10 ka and more gradual RSL fall in the Holocene.

East Trondheimsfjord sea level, as recorded in 24 isolation ba-sins and 1 sedimentary indicator (site 15, Fig. 6), followed a similar pattern (Nydal et al., 1964, 1985; Bondevik et al., 1997b; Kjemperud,

1986; Reite et al., 1982). From a peak altitude of 121.0 ± 1.8 m at 13.7ka, sea level fell without transgression through the Holocene, with rates before 9.6 ka exceeding ~2 cm/yr and after remaining at ~0.5 cm/yr.

4.8. Northern møre og romsdal, sites 16-17

The Northern Møre og Romsdal RSL database, principally from Frøya (site 16, Fig. 6) and Hitra (site 17, Fig. 6), is derived solely from isolation basins and consists of 15 index points, 5 terrestrial-limiting points, and 3 marine-limiting points (Svendsen and Mangerud, 1987; Solem and Solem, 1997; Solem et al., 1997; Kjemperud, 1986; Johansen, 1985). The highest isolation basin on Frøya places RSL at 34.1 ± 1.7 m at 12.2 ka (site 16). The remaining
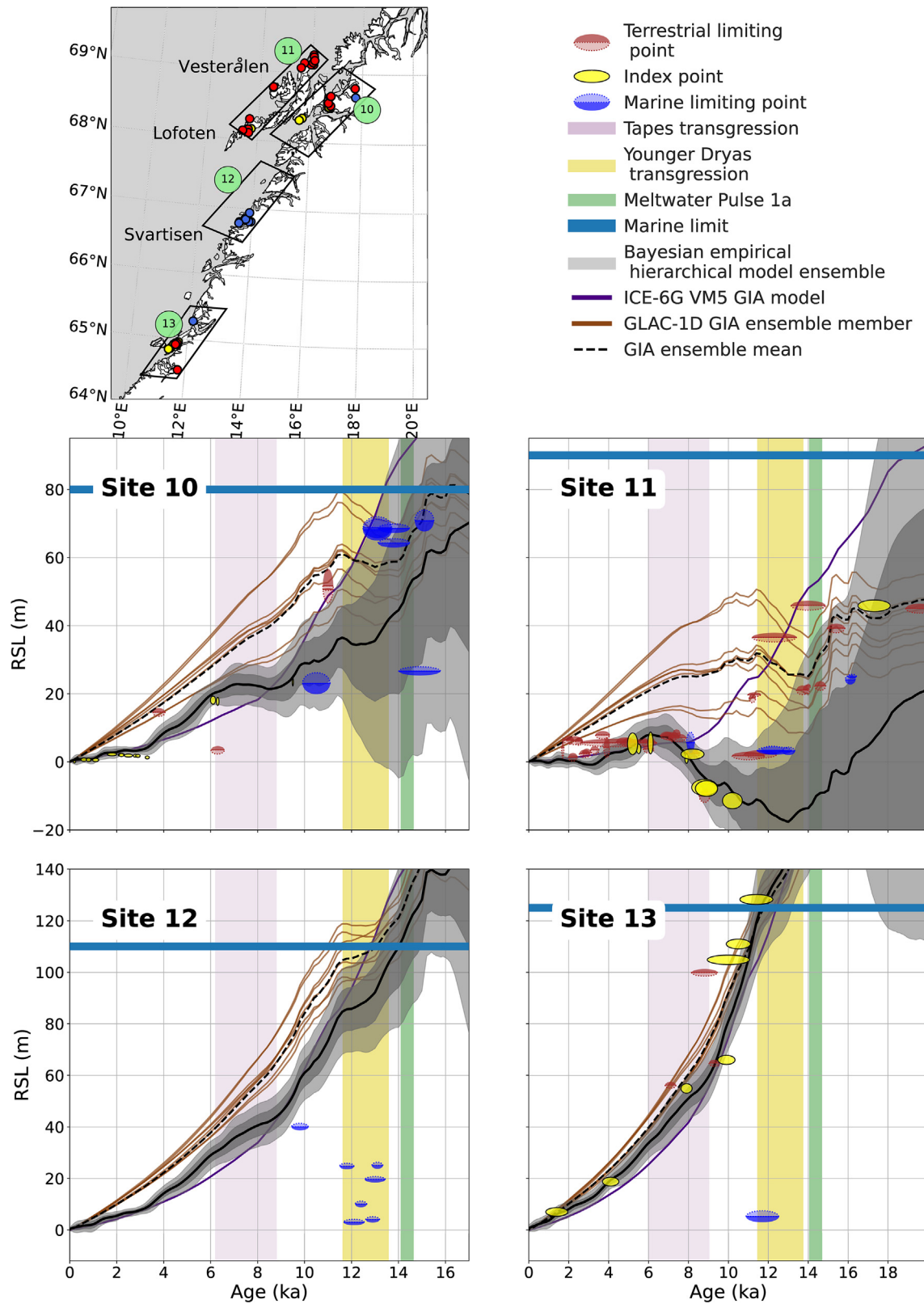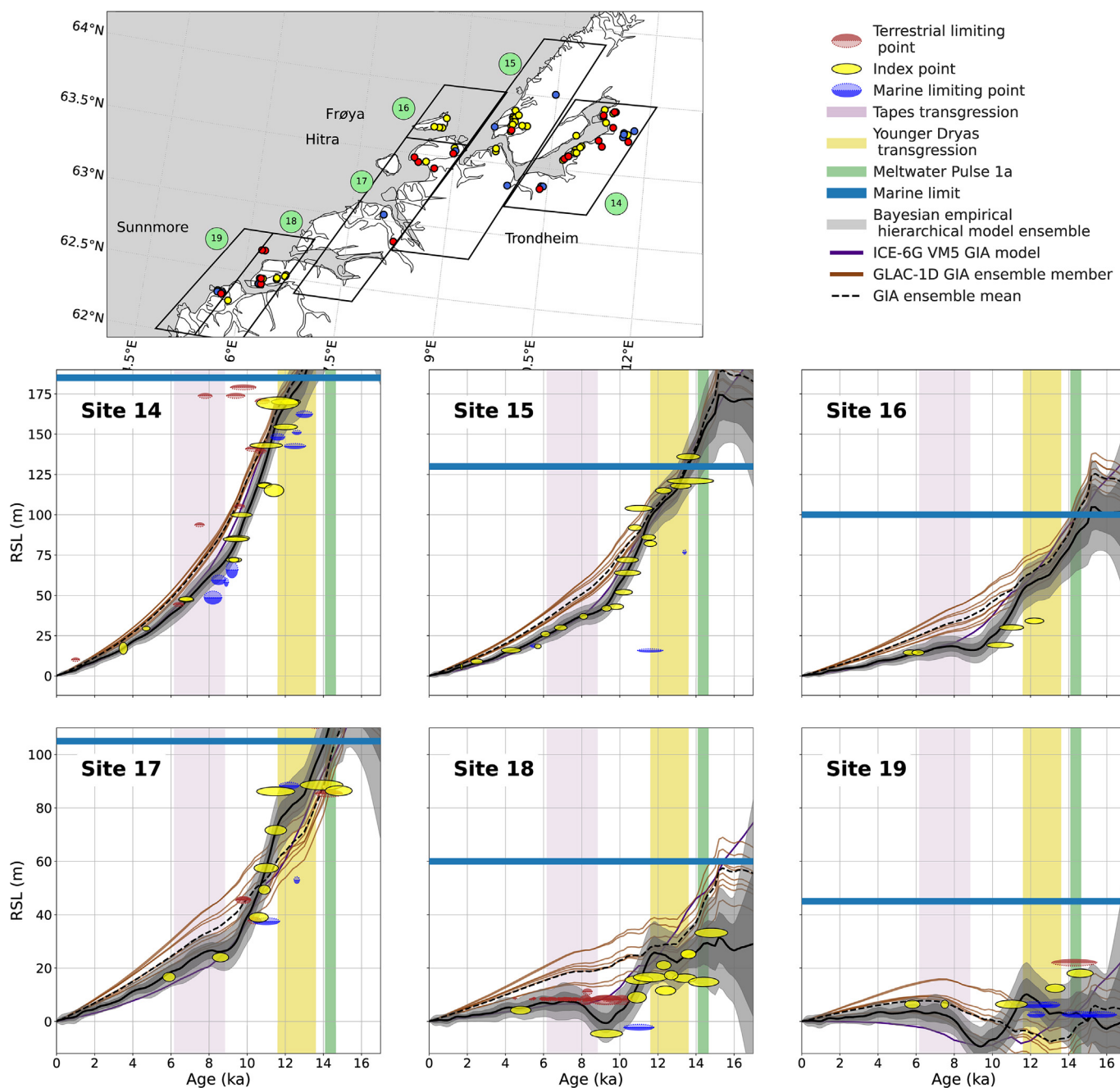
Fig. 5. Same as Fig. 3 but for central Norway: (10) southeast Vesterålen, (11) Northwest Vesterålen & Lofoten, (12) Svartigen, (13) Salten & Helgeland. See Fig. 3 caption for details.

Fig. 6. Same as Fig. 3 but for west Norway: (14) Inner Trondheimsfjord, (15) Outer Trondheimsfjord, (16) Frøya, (17) Nordmore, (18) Northeast Sunnmore, (19) southwest Sunnmore. See Fig. 3 caption for details.

index points have RSL decreasing gradually until 11.0 ka, falling rapidly for ~1 kyr, transgressing slightly, then declining linearly to present. Higher RSL data around 11 ka at sites 15 & 17 influence the STEHME prediction more strongly than this lower estimate at site 16, leading to a STEHME that updates towards the lower RSL index points in the early Holocene but remains higher than the Frøya index points. The STEHME also records a small Tapes transgression at this coastal site.

On Hitra (site 17), isolation basin index points trace RSL plateauing around 86.0 ± 1.7 m between 14.8 ka and 11.5 ka. After that, the rate of sea-level fall increased sharply for 1.5 kyr before slowing after 8 ka, transgressing less than a meter, then falling steadily to the present (Solem et al., 1997; Solem and Solem, 1997; Kjemperud,

1981b,a; Johansen, 1985; Svendsen and Mangerud, 1987). The STEHME shifts upwards to pass through the YD index points, then falls sharply to intersect with the middle Holocene index points.

4.9. Sunnmore, sites 18-19

Sea-level isolation basin data from Sunnmore in southern Møre og Romsdal, including 13 index points, 90 terrestrial limiting data, and 1 marine limiting datum (site 18, Fig. 6), outline a deglacial RSL regression that likely passed 33.2 ± 1.7 m at 14.8 ka, slowed or transgressed between 13.3 and 11.9 ka, then regressed to reach −3.0 ± 1.5 m at 9.3 ka (Svendsen and Mangerud, 1987; Nydal et al., 1972; Bondevik et al., 1997a; Lie et al., 1983; Lise Kristiansen
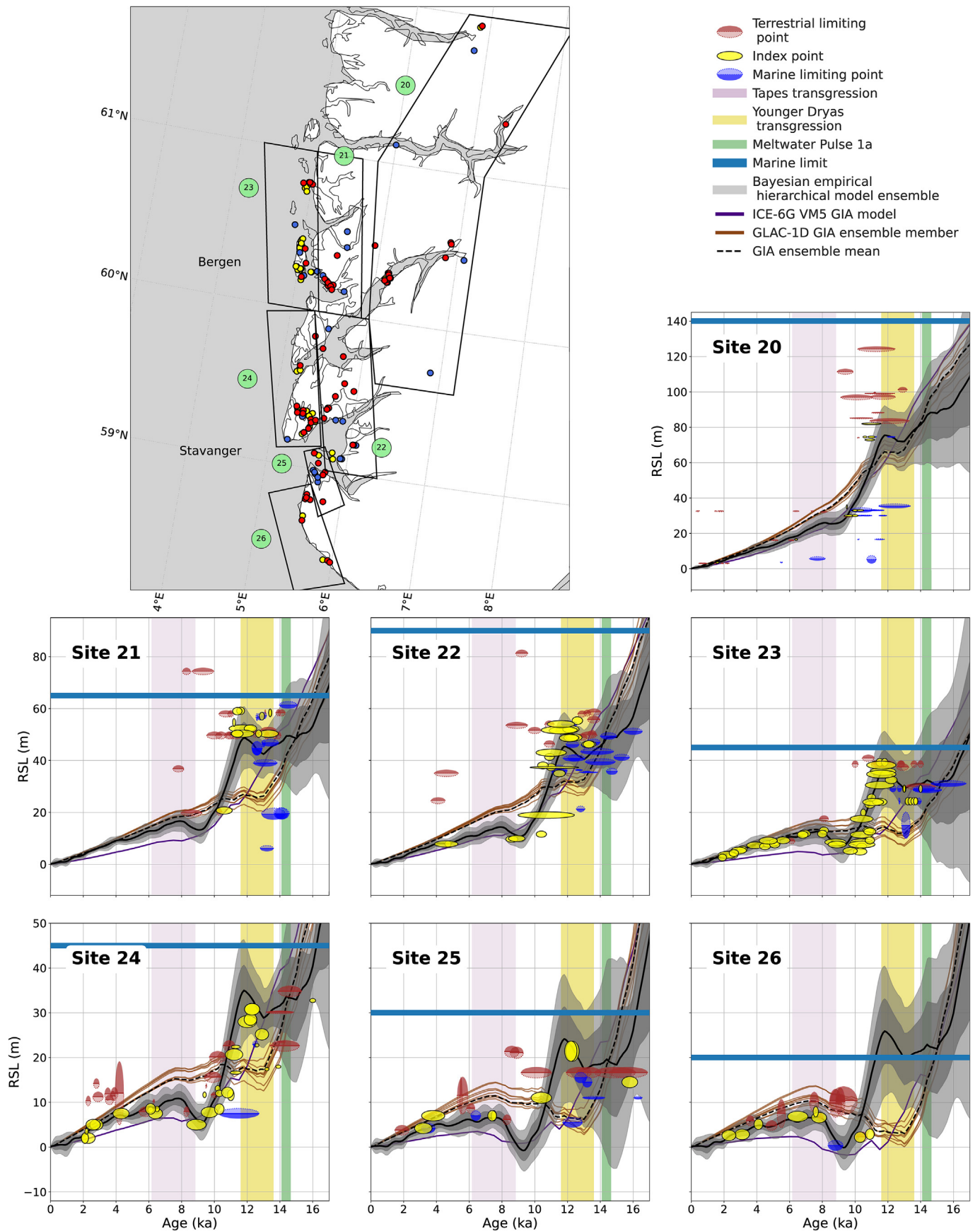
Fig. 7. Same as Fig. 3 but for southwest Norway: (20) inner Hardanger-, Sogne-, and Innvikfjord, (21) Inland Sunnhordland, (22) Northeastern Boknafjorden, (23) Bergen, (24) North Rogaland, (25) Stavanger, (26) Southwest Rogaland. See Fig. 3 caption for details.

et al., 1988; Bondevik et al., 2019). Sea level transgressed after that with an isolation datum that places Sunnmore RSL at 8.6 m by 4.5 ka, before RSL fell to its present-day level. The STEHME is consistent with both the YD RSL slowdown or transgression and the mid-Holocene transgression. Abundant RSL indicators at this site and in the surrounding region (sites 21−25, Fig. 7) keep the STEHME uncertainties low, and the single index point at 9.3 ± 1.2 ka delimits the onset of the Tapes transgression at this site.

In southwesternmost Sunnmore (site 19, Fig. 7), 11 isolation basin indicators—5 index points, 5 marine-limiting points, and 1 terrestrial limiting datum—place RSL at 18.0 ± 1.6 m at 14.6 ka (Bondevik et al., 1997b, 1998; Svendsen and Mangerud, 1990). Index points also constrain sea level to reach 6.4 ± 1.5 m by 7.5 ka, remain there until 5.8 ka, then regress to the present. As at site 18, the STEHME's spatial covariance produces a posterior model that accords with the observations within uncertainty.

4.10. Hardangerfjord, site 20

The sea-level history of Inner Hardanger, Sogne, and Innvik fjords (site 20, Fig. 7) is delimited by 67 indicator data consisting of 19 index points (including 9 isolation basins), 19 marine-limiting points, and 29 terrestrial-limiting points (Romundset et al., 2010a; Helle, 2006). Index points place sea level at 82.7 ± 0.6 m at 10.7 ka, then track a rapid fall to 32.0 ± 0.6 m at 9.5 ka. During the Holocene, the rate of sea level fall slowed to a possible sub meter-scale transgression; RSL then regressed continuously through 18.5 ± 0.6 m at 6.4 ka and towards the present. High index points lift the STEHME curve in the early Holocene, but because of data scarcity, the model assigns a low probability to a sea-level transgression reaching 81 m at this site. Some evidence (e.g. Helle et al., 1997) suggests that the YD transgression reached as high as 117 m in this region. The isolation basin sediments recording this elevation, however, are typically disturbed, yield conflicting radiocarbon dates, or contain anomalously old Allerød carbon (Mangerud et al., 2016). These data are therefore labeled terrestrial-limiting or discarded.

4.11. Bergen, site 21

The sea-level record around Bergen in inland Sunnhordland (site 21, Fig. 7) indicates that RSL transgressed in the late deglacial (12.8−10.9 ka, Lohne et al., 2004; Bondevik and Mangerud, 2002; Nydal et al., 1970; Nydal, 1960; Gulliksen et al., 1978). Sea level, as constrained by 16 index points, 14 terrestrial-limiting points, and 19 marine-limiting points, dips below 50.3 ± 1.3 m at 13.3 ka and rises to 59.1 ± 1.2 m by 11.6 ka. The youngest index point at site 21 places RSL at 20.7 ± 1.2 m at 10.6 ka. The STEHME is constrained by data at site 23 to pass through ~28 m at 13.3 ka (site 23) and also to pass through the 13.3 ka data at sites 21 and 22 at ~45 m — sites within 80 km of each other.

Though the STEHME 95% credible envelope includes nearly all index points in this region, the model's spatiotemporal length scales of covariation do not permit such short-scale variability, and the model mean passes between the two YD constraints. A gap in RSL data during the mid-Holocene precludes data-driven certainty about the existence or magnitude of a Tapes transgression in the Bergen region. Because of covariation from surrounding sites, however, the STEHME produces a Tapes transgression centered around ~7 ka.

4.12. Inner boknafjorden, site 22

A similar sea-level pattern emerges in Northeastern Boknafjorden (site 22, Fig. 7). Deglacial isostatic rebound in Boknafjorden is punctuated by a ~12 m transgression starting at 13.3 ka and ending at 11.8 ka (Kaland, 1988; Anundsen and Fjeldskaar, 1983; Anundsen, 1978). Isolation basin records from the Stavanger archipelago then indicate that sea level fell ~40 m in 3.6 kyr (to 13.7 ± 1.2 m at 10.4 ka) and returned to that level at 4.6 ka before regressing to present-day levels (Prøsch-Danielsen, 1993). As around Bergen, the STEHME mean captures a YD transgression, but the full magnitude of the transgression, as outlined by index points, is only contained within the STEHME's uncertainty envelope.

4.13. Sunnhordland, site 23

Sea level in Sunnhordland is delimited by 86 indicator points. In Austrheim and the Sotra archipelago (site 23, Fig. 7), 57 isolation basin index points, supported by 19 terrestrial-limiting and 8 marine limiting points, record that after a ~5 m regression between 13.9 and 13.5 ka, RSL transgressed 12 m to reach a maximum of 39.3 ± 1.2 at ~11.8 ka, then fell at 3.3 cm/yr to 6.7 ± 1.5 m at 10.3 ka (Lohne et al., 2007; Bondevik et al., 1997a, 2006; Kaland, 1984; Krzywinski and Stabell, 1984; Gulliksen et al., 1975; Nydal, 1960). In the mid-Holocene, indicators suggest that Sunnhordland sea level transgressed to 12.8 ± 1.5 m by 8.1 ka then fell to present-day levels. The data drive the STEHME to include substantial YD and Tapes transgressions that are consistent with the data.

### 4.14. Northern Rogaland, site 24

Sea level in North Rogaland (site 24, Fig. 7) including Karmøy, Tysvaer, Fosen, and Haugesund, is well-documented by 48 indicator points, including 30 isolation basin index points; 23 terrestrial limiting points from sedimentary, archeological, and isolation basin indicators; and 3 marine-limiting data from marine terraces and isolation basins (Midtbø et al., 2011; Kaland, 1984; Thomsen, 1989; Helle et al., 2007; Johnsen, 2017; Austad and Erichsen, 1987; Vasskog et al., 2019; Karlsen, 2009; Lindblom et al., 1997). Northern Rogaland SLIPs track a RSL history that falls from LGM to 17.4 ± 1.1 m at 13.9 ka (Johnsen, 2017; Thomsen, 1989). It then rises to 30.8 ± 1.2 m by 11.7 ka (Thomsen, 1989) before falling sharply to its minimum at 5.0 ± 1.2 m at 9.4 ka. In the Holocene, index points suggest that RSL in Northern Rogaland advanced to a maximum of 8.5 ± 1.2 m by 6.5 ka, then retreated to the present (Kaland, 1984; Thomsen, 1989; Midtbø et al., 2011; Prøsch-Danielsen, 2006). The STEHME aligns with the YD maximum RSL and the Tapes transgression in form and amplitude. High RSL index points from sites 22 & 23, however, prevent STEHME RSL from falling to ~16 m at 13.3 ka, as the data indicate occurred.

4.15. Stavanger, site 25

The RSL records near Stavanger extend the Holocene RSL curve into the deglacial with isolation basin index points that bracket a YD transgression (site 25, Fig. 7). Stavanger sea-level indicators suggest that RSL first dipped below 14.5 ± 1.3 m at 15.8 ka, transgressed to 21.4 ± 2.2 m by 12.3 ka (Prøsch-Danielsen, 1993; Thomsen, 1982; Helle et al., 2007), fell below 4.7 ± 1.1 m by 8.4 ka (Juhl, 2001), rose as high as 10 m in the mid-Holocene ((Prøsch-Danielsen, 2006; Bang-Andersen, 1995), then fell to the present (Gulliksen et al., 1975; Prøsch-Danielsen, 2006). Within uncertainties, the STEHME is consistent with this history, but the model mean does not pass through the oldest SLIP because of higher nearby data of similar age (sites 22 & 23).

4.16. Southwest Rogaland, site 26

In Southwest Rogaland (site 26, Fig. 7), sea level is constrained
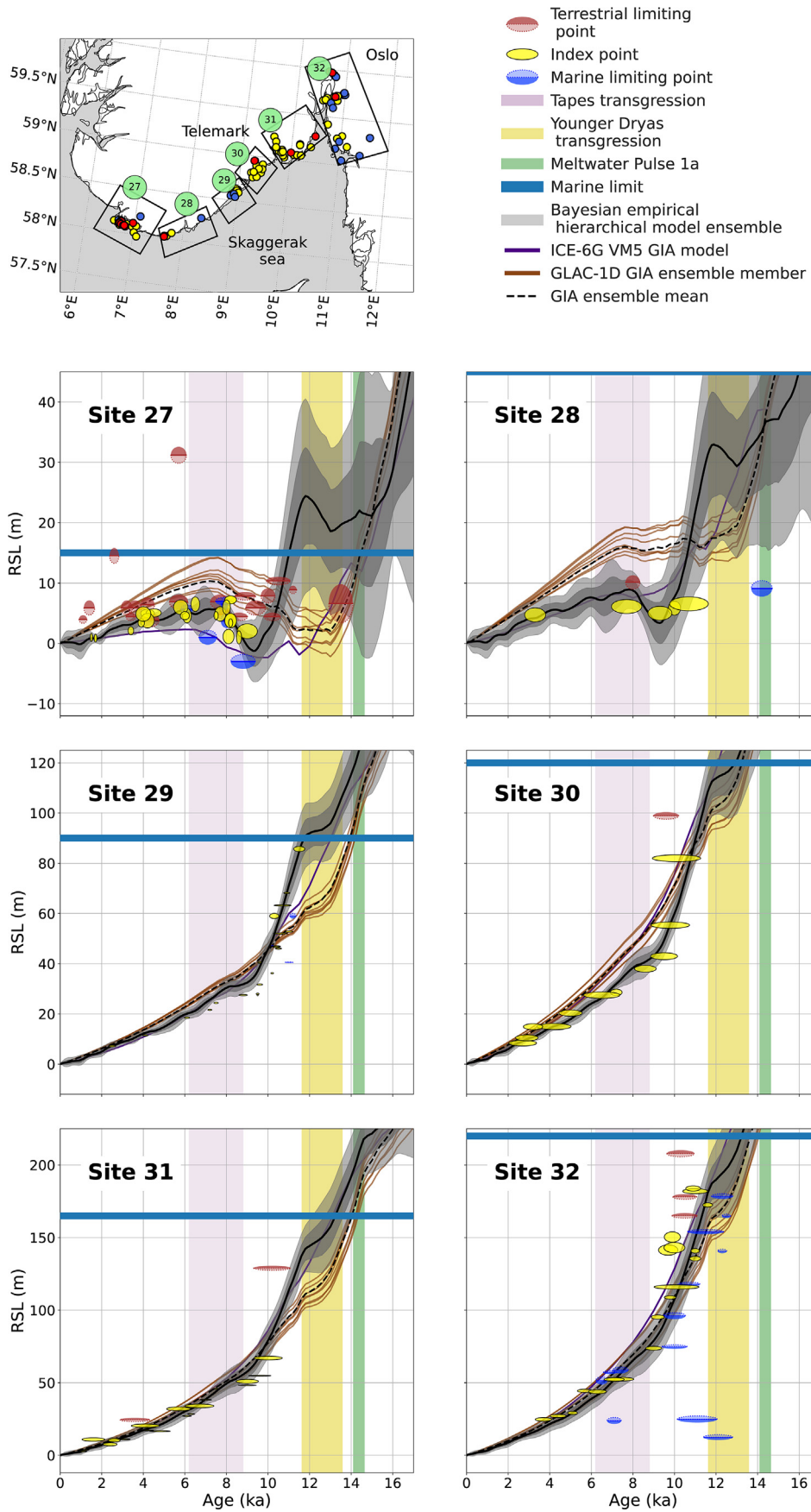
by peat bog index points to reach ~ 2.9±1.2 at 10.9 ka, transgress to 7.9 ± 1.1 m by 7.6 ka, and slowly fall to the present (Prøsch-Danielsen and Simonsen, 2000; Gulliksen et al., 1975; Thomsen, 1983; Prøsch-Danielsen, 2006; Juhl, 2001; Nydal, 1960; Simonsen, 2005). The STEHME reproduces the Tapes transgression present at site 26 and accords with earlier data given large uncertainties. Spatial covariance in the STEHME extends the YD transgression to this site despite a lack of data prior to 11 ka.

4.17. Skagerrak coast: Vest-Agder, sites 27-28

In Vest-Agder (site 27, Fig. 8), sea level is constrained by 21 index points and 15 terrestrial-limiting points from isolation basins, supported by six marine-limiting marine terrace data and three terrestrial-limiting peat bogs (Romundset et al., 2015; Nydal et al., 1970; Nydal, 1959, 1960, 1962; Hafsten and Tallantire, 1978; Hafsten, 1983; Hoeg, 1995; Prøsch-Danielsen, 1996, 1997). In Lista, index points suggest that sea level reached a minimum of 2.0 ± 1.2 m at 9.0 ka, rose to exceed 6.5 ± 1.3 m by 6.5 ka, then fell through the rest of the Holocene. The lack of pre-Holocene index data in Vest-Agder leaves the STEHME in the YD under-constrained, but the model accurately captures the Tapes transgression.

The oldest SLIP records in Hartmark (site 28, Fig. 8) indicate that RSL reached 6.6 ± 1.2 m at 10.7 ka and remained constant for at least 2 kyr (Nydal, 1959, 1962). There is then a hiatus in index points until 3.3 ka, when sea level passed 4.7 ± 1.2 m on its way to the present. Though many high RSL data exist to the east (e.g. sites 29 & 30), the few index points here are sufficient to diminish the magnitude of the STEHME-modeled Tapes transgression to ~5 m.

4.18. Skagerrak coast: Aust-Agder, site 29

Further north along the Skagerrak coast (site 29, Fig. 8), the RSL history at Tvedestrand, Aust-Agder, is tightly constrained by 21 index and 3 marine limiting points from isolation basins (Romundset et al., 2018). From a maximum of 85.7 ± 1.0 m at 11.5 ka, sea level regressed to 27.5 ± 0.3 m by ~9.5 ka, then fell more slowly until present-day levels. The majority of data fall within the STEHME's 95% credible envelope.

4.19. Skagerrak coast: telemark, sites 30-31

The RSL history of Telemark (sites 30 & 31, Fig. 8) is delimited by 20 index and 2 terrestrial-limiting isolation basin data. At Kragerø (site 30), index points outline a rapid RSL regression from below 82.2 ± 1.4 m at 10.1 ka to 43.0 ± 1.2 m at 9.5 ka, then a slower regression through the rest of the Holocene (Stabell, 1980). At Porsgrunn (site 31), index points suggest that sea level fell continuously through the Holocene from 67.0 ± 1.3 m at 10.0 ka through 32.0 ± 1.2 m at 5.7 ka to the present (Nydal, 1960; Stabell, 1980; Henningsmoen et al., 1978; Sørensen et al., 2014).

4.20. Skagerrak coast: Oslo & East Viken, site 32

RSL index points from 13 isolation basins, supported by 5 isolation basin terrestrial-limiting points and 11 marine-limiting data from marine terraces and peat bogs (site 32, Fig. 8), constrain the sea-level history in Oslo and along the eastern side of Oslofjorden (Sørensen, 1979; Nydal et al., 1970, 1985; Nydal, 1960; Gulliksen et al., 1975). From a highest index point at 172.4 ± 1.2 m at 11.6 ka, indicators track a continuous sea level fall to the present,

with RSL falling most rapid in the early Holocene — ~116 m in 1.6 kyr — and slower through the late Holocene.

5. Discussion: spatiotemporal patterns of RSL change

Norwegian RSL change over the last 20 kyr has been dominated by postglacial rebound (Fig. 9A), which was interrupted by the YD and Tapes transgressions. While Fennoscandian GIA models capture the rebound (Lambeck et al., 1998; Steffen and Wu, 2011; Patton et al., 2017), they produce the transgressions to varying degrees, highlighting inconsistencies in ice sheet reconstructions and/or Earth viscosity models.

RSL in northern Norway tends to be overestimated by the GIA ensemble compared to our STEHME prediction (Fig. 9C), while in southern and southwestern Norway, GIA ensemble members do not capture the YD transgression and predict Tapes transgressions that are of smaller amplitude and differing durations than that of the STEHME. These misfits are likely produced by inaccuracies in solid earth structure, including unaccounted-for lateral variations in mantle viscosity and lithospheric thickness. They may also be caused by inaccuracies in ICE-6G and GLAC-1D EIS ice volumes. Estimates of both pre- and post-LGM EIS evolution differ substantially (Näslund et al., 1994; Lambeck et al., 2006, 2010; Patton et al., 2017), and differences in glacial-phase loading history can have a large effect on postglacial GIA predictions near the EIS (e.g. Auriac et al., 2016, Fig. 9).
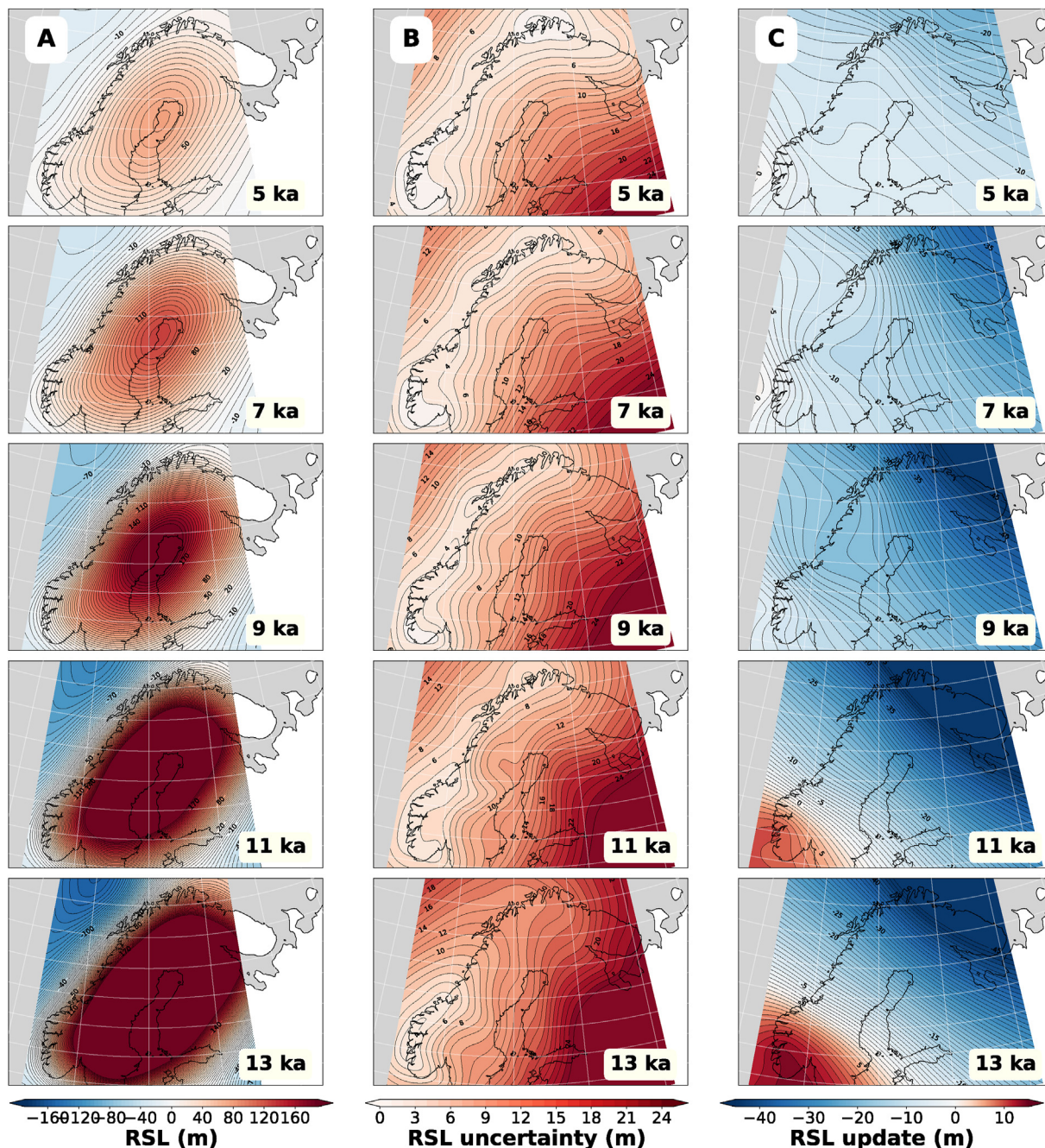
A comprehensive exploration of which ice sheet-solid earth combinations best fit the Norwegian sea-level database is beyond the scope of this study, as is constructing a STEHME that uses GIA prior predictions from large ensembles of ice histories and solid earth structures. Nevertheless, we show that a prior GIA ensemble composed of nine GIA predictions from two contrasting ice sheet histories is sufficient to produce a STEHME RSL field across Norway that is consistent with the vast majority of Norwegian RSL data and reproduces both the YD and Tapes transgressions.

In order to produce the observed transgressions, the mean of our STEHME is higher during the YD, falls more rapidly after the YD, and traces RSL change in the mid-Holocene that has a shorter period but higher amplitude than the mean of the GIA ensemble (Figs. 9C and 11 ka; 7, sites 23−26, respectively). The spatiotemporal smoothness of the STEHME's posterior and uncertainty is explained by the model's spatial and temporal covariation length scales (Fig. 1A and B, respectively), which cause the model to update the GIA prediction even in areas distant from RSL data, with the uncertainty of that update increasing with distance from the nearest observation.

In the following sections, we will describe and investigate the origin of the two transgressions using our data compilation and STEHME prediction.

5.1. Younger Dryas transgression

During the late deglacial, southwestern Norway underwent a local RSL transgression that lasted ~2 ka and reached a maximum amplitude of ~10 m in the 250 km stretch of coastline between Stavanger and Fonnes (Figs. 7 and 8, sites 21−25). Beyond this region, RSL fall during the YD also slowed between 13.5 and 11 ka in Trondheimsfjord (sites 14−15, Svendsen and Mangerud, 1987) and along the Skagerrak coast (site 29, Romundset et al., 2018). A deglacial RSL rise during the YD was also seen across areas of northern hemisphere glaciation in Iceland and Canada. For

Fig. 8. Same as Fig. 3 but for south Norway: (27) Vest-Agder, (28) Kristiansund, (29) Aust-Agder, (30) Kragerø, Telemark, (31) Porsgrunn, Telemark & Vestfold, (32) Oslo & East Viken. See Fig. 3 caption for details.

Fig. 9. Time slices at 2 kyr timesteps of the Bayesian empirical hierarchical model ensemble (STEHME, column A), the STEHME 95% credible interval (column B), and the difference between the mean of the GIA model ensemble and the posterior mean of the STEHME, i.e. the mean of the amount that the STEHME updates the GIA models in order to better fit the Norwegian RSL record (column C). Blue regions in (C) are places where the STEHME mean has lower RSL than the GIA ensemble mean, red, where the STEHME mean has higher RSL. Contours are 5 m (A), 1 m (B), and 1 m (C). (For interpretation of the references to color in this figure legend, the reader is referred to the Web version of this article.)

instance, sectors of Iceland likely underwent a YD transgression of at least 10 m (Rundgren et al., 1997; Pétursson et al., 2015). Limiting data from around the Innuitian Ice Sheet near Fosheim peninsula also indicate that RSL reached a maximum before 10.6 ka with a suggested transgression in the late deglacial (England, 1992; Bell, 1996). In both instances, the proposed cause of sea-level transgression is a local ice sheet readvance.

The driver for the YD transgression in Norway is similarly thought to be a readvance of the EIS some time during the late Bolling-Allerød and YD periods (Lohne et al., 2007; Helle et al., 2007; Mangerud et al., 2016). The timing of the YD ice sheet readvance varied around Norway. As dated by YD end-moraines, ice-sheet lobes in the north (Troms), center (Trøndelag), and east (Oslo) reached maxima in the early-mid YD, whereas in the southwest the EIS likely reached its maximum in the latest YD (Hughes et al., 2016; Mangerud et al., 2016). The magnitude of these readvances is difficult to discern because the advancing ice sheet destroyed evidence of its earlier retreat, but extant evidence suggests that the southwest EIS readvance was larger than analogues further north (e.g. Knies et al., 2007). This readvance is not included in standard global ice models (e.g. GLAC-1D, ICE-6G; Abe-Ouchi et al., 2015; Peltier et al., 2015) but is included in some regional

models (e.g. Patton et al., 2017; Fjeldskaar and Amantov, 2018).

EIS readvance would have raised RSL through a combination of increased gravitational attraction and local subsidence due to ice loading. Though the duration and magnitude of these effects would depend on the amount of ice change and the solid earth structure underlying the region, estimates from GIA modeling suggest that between 13 and 11.6 ka EIS readvance diminished isostatic uplift in parts of southwest Norway by as much as 25 m, while the increase in gravitational attraction raised RSL by less than 1 m (Fjeldskaar and Amantov, 2018). Recent tomographic studies in Norway suggest a strong northeast-southwest gradient in seismic wave speed along the Norwegian coast, which likely translates into temperature and mantle viscosity (e.g. Barnhoorn et al., 2011; Schoonman et al., 2017; Lei et al., 2020). Though a cold continental root underlies much of Scandinavia, asthenospheric fingers radiating from the Iceland plume may have weakened the earth structure beneath southern Norway (Rickers et al., 2013). A weak lithosphere and low-viscosity asthenosphere beneath southern Norway also match regional paleoshoreline tilts and accord with GIA-based assessments that a viscosity gradient beneath Fennoscandia is needed to fit GPS uplift rates and RSL records simultaneously (Fjeldskaar and Amantov, 2018; Whitehouse et al., 2006; Steffen and Kaufmann, 2005). Weak Earth structure would have sped the solid earth response time to YD readvance, as happened beneath Iceland during the deglaciation (Sigmundsson, 1991).

A paucity of northern Norwegian YD sea-level records, and longstanding evidence for halts in EIS ice recession along the northern coast of Norway (Sollid et al., 1973), make it challenging to rule out a YD transgression in coastal Finnmark, Troms, and on the Varanger peninsula based on sea-level data alone (sites 1−6 & 9, Figs. 3 and 4). Moreover, recent estimates of Barents Sea deglaciation timing, which place local ice retreat in Finnmark at ~14.6 ka (Romundset et al., 2011), do not themselves preclude a YD transgression there, because the region would have been ice-free during the YD interval. However, limiting data in Finnmark and Troms (sites 7 & 8, Figs. 3 and 4), when combined with marine limits, imply that no transgression is recorded inland in north Norway.

Further south in the Lofoten-Vesterålen region (sites 9 & 10, Figs. 3 and 5), the combination of index and limiting points also preclude a YD transgression. More data from Finnmark and Troms are needed to clarify whether the YD transgression occurred north of the northernmost extant sea-level evidence for such a transgression, which occurs in coastal Trondheimfjord in the form of a sea-level slowdown between 14 and 12 ka (site 15, Figs. 5 and 6). On the south coast of Norway, by contrast, the STEHME produces a YD transgression as large as 8 m (Figs. 9C and 11 ka), which argues for the existence of an ice sheet readvance as well as possible weaker solid-earth structure. With RSL data alone it is not possible to tell whether weak earth structure or differential EIS readvance magnitude caused the differences between north and south Norwegian YD sea-level histories, but it seems likely that both mechanisms may have contributed to the observed pattern.

We estimate the magnitude, timing, and duration of the YD transgression using the STEHME's continuous sea-level field. We map these fields, as well as the difference between STEHME and GIA ensemble maximum amplitudes, by computing inflection points in mean RSL between 14−12.3 ka and 12.3−11 ka, which are the intervals that flank the pre-YD transgression minimum and YD maximum (Fig. 10, Fjeldskaar and Amantov, 2018). The STEHME transgression reaches a maximum at around 11.8 ka (Fig. 10C), with a maximum amplitude increasing from ~1 m at inland sites to >8 m along the southwestern Norwegian coast. Though the maximum amplitude of the STEHME YD transgression exceeds that of the GIA ensemble mean at the vast majority of mapped sites (Fig. 10B), data-model comparisons (Fig. 7 site 23, 24) suggest that the STEHME still underestimates the YD transgression amplitude at some coastal sites and that Fig. 10A should therefore be considered a minimum estimate. Data paucity between Sunnmore and Bergen (Fig. 2) also leads the STEHME to predict no YD transgression in that region. This result is discordant with the sea-level effects predicted by regional modeling of ice dynamics (Fjeldskaar and Amantov, 2018), which indicates that further observations of YD-age RSL indicators between Sunnmore and Bergen are needed.

The STEHME produced here — like other single STEHMs
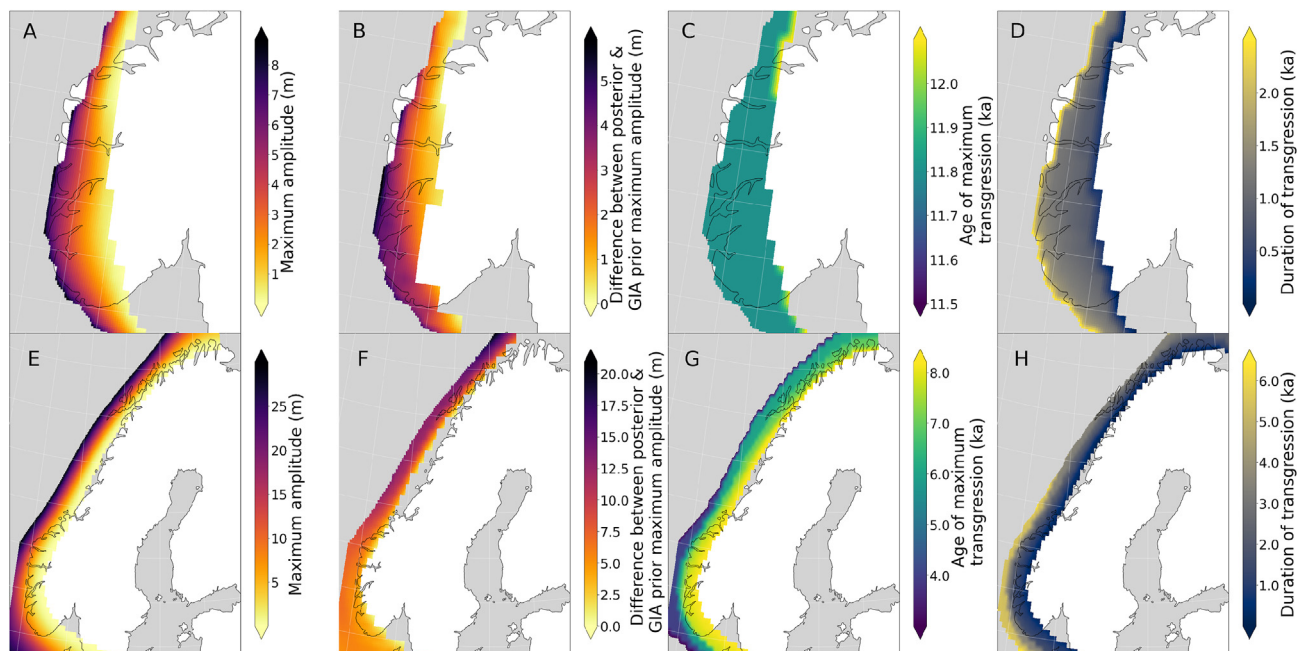
Fig. 10. Maps of the maximum amplitude (A, E), difference between posterior and GIA ensemble mean prior maximum amplitude (B, F), age of sea-level maximum (C, G), and duration (D, H) of the Younger Dryas (A−D) and Tapes (E−H) transgressions based on the STEHME.
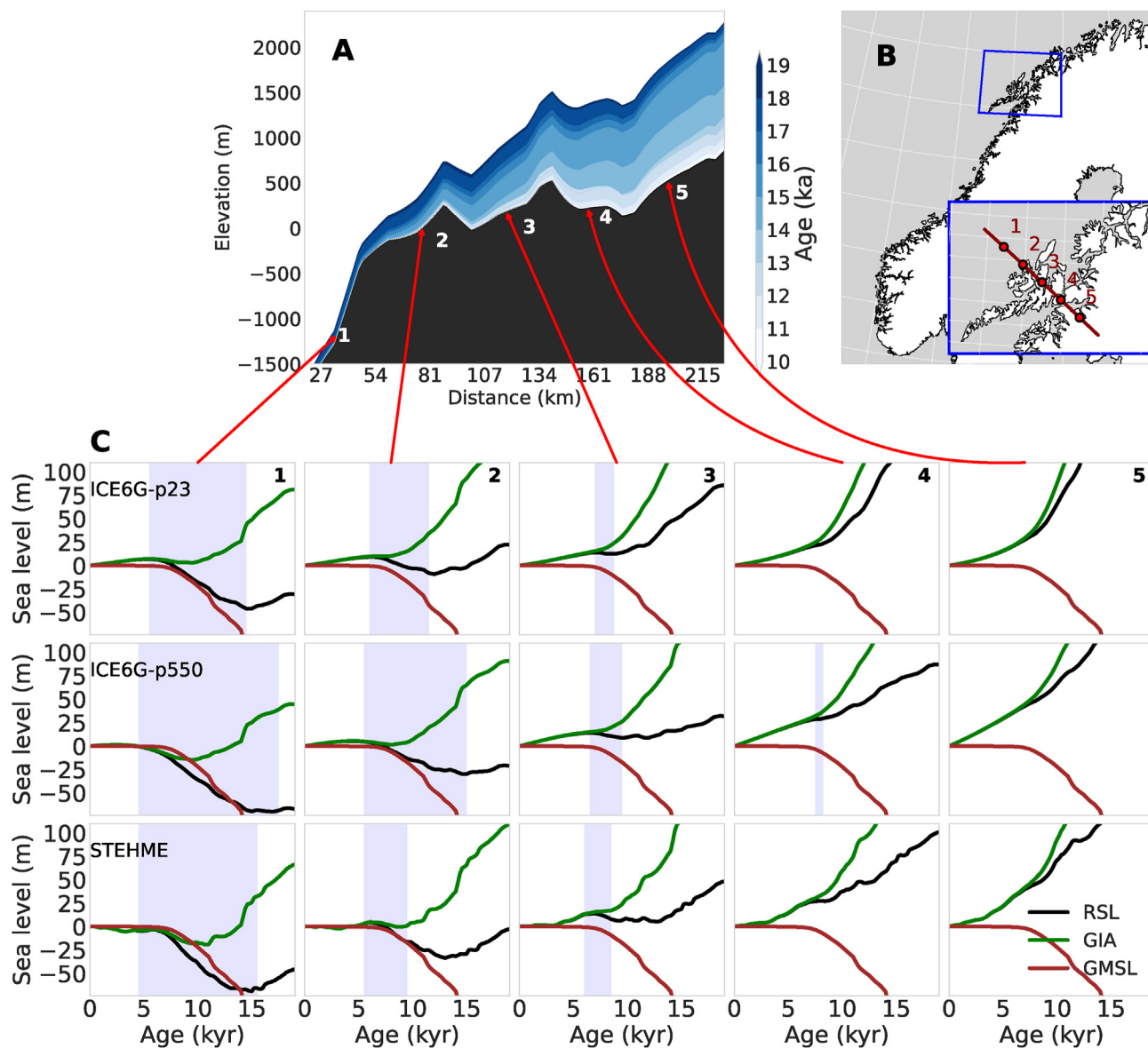
Fig. 11. Elevation profile across the Lofoten-Vesteralen archipelago of ICE-6G ice thicknesses 19–10 ka (A); Location of transect (B); Time series plots of predicted relative sea level (RSL, black), global mean sea level (GMSL, red), and glacial isostatic adjustment (GIA, green) for the STEHME and ICE-6G with 96 km lithosphere and two contrasting mantle viscosity structures: weak (2×10^{20} Pa s upper mantle, 3×10^{21} Pa s lower mantle) and strong (5×10^{20} Pa s upper mantle, 50×10^{21} Pa s lower mantle). GIA in panels 1–5 of top two rows is computed by subtracting ICE-6G GMSL from ICE-6G RSL. GIA in bottom row is computed by subtracting ICE-6G GMSL from STEHME posterior mean. Blue highlight denotes duration of modeled Tapes transgression (C). (For interpretation of the references to color in this figure legend, the reader is referred to the Web version of this article.)

produced by the post-glacial sea-level modeling community — assumes that a single set of spatiotemporal processes forms Norway's 'true' sea level, that sea-level covariation decays with distance, and that covariation does not depend on location or time (Ashe et al., 2019). Models of this nature are ill suited for processes that operate only in certain regions or time intervals, change smoothly in some places but abruptly in others, or whose covariation decouples from distance — e.g. intrahemispheric teleconnections or GIA sea-level fingerprints. Norwegian RSL data record two such abrupt sea-level discontinuities, both in southwest Norway. Neither of them is fully captured by the STEHME. The first occurs near North Rogaland (site 24, Fig. 7). There the amplitude of the YD transgression diminishes by > 10 m across the ~20 km Boknafjorden (sites 24, 25, 26). The second occurs between Bergen and Hardangerfjorden, where >10 m differences exist between pre-YD transgression RSL minima at sites 21 (48 m) & 23 (24 m) vs. sites

22 (45 m) & 24 (16 m) as outlined by SLIPs. In both cases, the regional covariance structure to which the STEHME optimizes—average length scale of 3000 km and temporal scale of 2.5 kyr—is too long to fully model the rapid spatiotemporal fluctuation that the sea-level data require. The latter discontinuity may, as Helle et al. (2007) argued, be up-to-the-East tectonic displacement produced by one of the many sizeable postglacial Norwegian earthquakes (Arvidsson, 1996; Lagerbäck and Sundh, 2008; Sutinen et al., 2014). The former discontinuity is likely caused by ice sheet readvance and not tectonics (Mangerud et al., 2016). Though other disjointed sea-level records have not to our knowledge been reported elsewhere in Norway, the postglacial seismic activity ubiquitous along the Norwegian coastline (c.f. Olesen et al., 2013) suggests that higher resolution sea-level observations in northern and central Norway could uncover additional discontinuities.

For locations like southwest Norway, a nuanced form of sea-

level modeling is needed, one that can accommodate sea-level processes whose covariance length scales change through space and time. Though the ensemble approach used here satisfies that need by permitting a range of length scales of covariation, the computational cost of producing ~9000 STEHMs suggests that other approaches, such as the use of anisotropic kernels, may be more feasible for future studies of sea level that seek to include such abrupt RSL discontinuities. The implementation of a model with those characteristics is beyond the scope of this paper, but the application of models with anisotropic kernels is established in the GPR (e.g. Saatchi et al., 2010; Grande et al., 2016) and Bayesian change point communities (e.g. Shaochuan, 2021), and is ripe for application to paleo sea-level studies.

5.2. Tapes transgression

A second major sea-level transgression in Norway occurred in the mid-Holocene, when RSL around the Norwegian coast rose up to 13 m (Fig. 10; Svendsen and Mangerud, 1987). Areas of Norway far from the center of the EIS record the most pronounced Tapes transgressions (e.g. sites 11, 26, 27; Kaland, 1984; Vorren and Moe, 1986; Prøsch-Danielsen, 2006; Lohne et al., 2007). By contrast, areas closer to maximum EIS loading do not record the transgression at all (e.g. sites 10, 13–17, 20, 29–32 Helle, 2006; Romundset et al., 2010b, 2018).

Because of good data-model fit during the Holocene, we used the STEHME's continuous sea-level field to calculate the timing and magnitude of the Tapes transgression. We map the maximum amplitude and duration of the STEHME Tapes transgression, along with the age of the sea-level maximum and the difference between STEHME and GIA ensemble maximum amplitudes, by calculating inflection points in mean RSL between 11–8 ka and 8–3 ka, which are the time windows that bracket the pre-Tapes transgression minimum and Tapes maximum (Fig. 10, Fjeldskaar and Bondevik, 2020). The transgression began around 10 ka and generally reached its maximum in the north around 6–7 ka and the south around 8 ka (Fig. 10G), though sparse records in northern Norway make the precise determination of the Tapes maximum more difficult (Romundset et al., 2010b, 2011, 2018). The STEHME predicts a Tapes transgression that occurs later and has consistently higher amplitude than that of the GIA ensemble (Fig. 10F). Early and regional studies from southwest Norway argued for the existence of two or multiple shorter Holocene transgressions (Fægri, 1944; Sørensen, 1985; Andersen, 1960), but the data aggregated here suggest a single transgression of longer duration.

Unlike the YD transgression, the Tapes transgression was not driven by local ice readvance because the EIS had melted by ~10 ka (Hughes et al., 2016). Instead, two other effects likely shaped the Tapes transgression: (1) a combination of concurrent GMSL rise and postglacial rebound such that GMSL rise briefly exceeds isostatic uplift near the edges of former ice sheets (henceforth termed the GMSL-GIA effect); and/or (2) peripheral bulge migration (PBM), which occurs in formerly glaciated areas when the hinge line separating areas of isostatic rebound from areas of peripheral bulge subsidence moves towards the center of the former ice sheet (Steffen and Wu, 2011). PBM is a phenomenon predicted by GIA theory and confirmed on the eastern edge of the EIS by increased eastern European river incision and sedimentation rates (Rosentau et al., 2007).

5.2.1. The GMSL-GIA effect

We investigate the extent to which the data support the GMSL-GIA effect by decomposing the observed and modeled RSL into contributions from GMSL and GIA with increasing distance from EIS loading (Fig. 11). Using the ice history ICE-6G and two solid earth

structures not used in the STEHME (two top rows of Fig. 11C) produces a transgression as a result of GMSL temporarily outpacing GIA. The magnitude of transgression and its duration are expected to increase with distance from the ice center while the maximum age is predicted to decrease. The transgression is larger and longer for a stiffer lower mantle due to a smaller GIA signal. These modeled predictions are in line with the observations (Figs. 10 and 11C).

If the GMSL-GIA effect is the dominant cause of the Tapes transgression, we would expect a transient transgression that would begin at most Norwegian coastal sites typically after 10 ka and likely no earlier than 11 ka, since 11–10 ka marked the final phase of EIS collapse and the beginning of purely viscous exponential decay in isostatic rebound along the Norwegian coast, as well as ongoing isostatic effects due to water loading (Hughes et al., 2016; Patton et al., 2017). This is consistent with our reconstruction, as can be seen in Figs. 4, 5, 7 and 8, in which both STEHME and RSL data place the earliest start of transgression around ~10 ka (site 26, 28) and the majority of transgression inceptions after 9.7 ka (e.g. sites 8, 18, 22, 23, 24, 27).

Further, if the GMSL-GIA effect is significant, the transgression should reach a maximum height before ~5 ka, since GMSL rose until the Laurentide ice sheet collapse ended around 7 ka and likely approached present-day levels by ~5–6 ka (Abe-Ouchi et al., 2015; Peltier et al., 2015; Lambeck et al., 2014; Bradley et al., 2016). Fig. 10F demonstrates this pattern, with the earliest transgression maximum modeled at ~8 ka and latest maximum along most of the coastline around 5 ka. Overall, we conclude that the correspondence between predicted and observed sea-level patterns suggests that the GMSL-GIA effect can explain much of the Tapes transgression.

5.2.2. Peripheral bulge migration

The second mechanism, PBM, could also contribute to a mid-Holocene transgression, but not to a subsequent regression. This would be the case for a site that first experiences isostatic rebound and then peripheral bulge subsidence as the hinge line moves closer to the Norwegian interior. Since topography is defined in GIA models as the negative of RSL, the pattern of solid-earth rise then fall corresponds to a pattern of RSL fall then rise, the timing of which would primarily depend on the timing of local ice margin retreat and the local solid earth structure. This pattern—regression-transgression with no subsequent regression—is not recorded at any coastal Norwegian site from which data have been collected, even though several with high data density (e.g. Fig. 5 site 11, Fig. 8 site 26) are the most probable locations to record such a pattern based on their distance from the center of EIS loading. It therefore is likely that every coastal Norwegian site is located inland of the EIS peripheral bulge hinge line and has been since the LGM. The site furthest oceanward in Fig. 11C, which underwent almost entirely regression and transgression with no subsequent regression, supports this hypothesis, as do maps of modern land uplift, which plot the present-day hinge line ≥50 km off the Norwegian coastline (e.g. Vestøl et al., 2019). We therefore conclude that PBM might have affected the magnitude of rebound and hence past sea level, but likely did not contribute to a reversal in the sea-level trend.

That may soon change. Isostatic uplift has until recently protected much of the Norwegian coastline from the effects of GMSL rise. Until the late 20th century, rates of land uplift in Norway, even in areas most distal to the EIS such as southwest Norway and the Lofoten-Vesterålen archipelago, exceeded rates of GMSL rise (Steffen et al., 2020; Dangendorf et al., 2019). In the last thirty years, however, rates of GMSL change have accelerated, while uplift is slowing down, causing RSL at some Norwegian sites to increase by as much as 2 mm/year (Simpson et al., 2015). As the EIS peripheral

bulge continues to migrate, this trend will continue: rates of GIA-related RSL fall for regions near the hinge line will decelerate until, as occurred for sites near the Laurentide (Batterson et al., 2003) and Greenland (Long et al., 2011) ice sheets during the Holocene, RSL fall ceases and the regions undergo RSL rise. The westernmost islands of the Lofoten-Vesterålen archipelago—already near the hinge line, as evidenced by their slow rates of RSL fall in the late Holocene—may soon begin to experience PBM-driven inundation. Most Norwegian sites, however, sit far enough from the hinge line that ongoing postglacial rebound will buffer them from future GMSL rise in the near-term (Simpson et al., 2012). At those sites, PBM would not have caused any transgression in the mid-Holocene but only a slowdown in regression which, only when combined with GMSL rise, produced the Tapes transgression. Though PBM is typically not cited in explanations of Tapes transgression dynamics (e.g. Fjeldskaar and Bondevik, 2020), further consideration of PBM dynamics in future work on Scandinavian sea level may help to clarify the RSL patterns observed on the Norwegian coastline.

5.2.3. Evidence for a mid-holocene transgression at other locations

A mid-Holocene RSL transgression of up to 10 m that interrupts the last deglacial RSL fall is a pattern observed in RSL records located along the edges of many former ice sheets. For instance, indicators from the St. Lawrence corridor of Canada's Maritime provinces record a highstand at ~5.5 ka that Vacchi et al. (2018) attribute to mid-Holocene ice sheet melt. Similar sea-level histories occurred on the edges of the British ice sheet in northern Scotland (Shennan et al., 2018); the Barents-Kara ice sheet in Franz Josef Land (Näslund et al., 1994); and the Cordilleran ice sheet in the south around Vancouver Island (Engelhart et al., 2015), off the coast of British Columbia (Shugar et al., 2014), and in the north off the Alaskan peninsula (Jordan, 2001). Spatiotemporal analysis such as performed in the study, along with further GIA modeling, could be used with sea-level data from these regions to better understand the influence of the GMSL-GIA effect and PBM on postglacial sea-level.

6. Conclusion

We have created the first comprehensive database of postglacial sea-level data that spans the Norwegian coastline and extends from 19.4 ka to the present. Derived from multiple sea-level indicators, including isolation basins, raised beaches, marine terraces, salt marshes, and peat bogs, the quality-controlled compilation contains 379 SLIPs and 418 limiting data, grouped into 32 regions based on similarity of uplift history and data availability. The majority of index points and limiting points were collected in the southern half of Norway and date to between 14 and 2 ka, with the highest concentration of index points occurring between around 11 and 5 ka. We expand on previous Norwegian RSL studies by assigning indicative meanings and standardized uncertainties to each indicator based on local RSL factors.

We employ an ensemble of empirical Bayesian hierarchical statistical models to produce probabilistic spatiotemporal assessments of Norwegian RSL over the last 16 kyr. Our model constrains rates and patterns of Norwegian RSL change produced by GMSL rise and Fennoscandian GIA response to Eurasian ice sheet collapse. In northeast and southeast Norway, RSL fell continuously between LGM and the present. Similar uninterrupted sea-level fall happened at every inland site around Norway. Along the south, southwest, and northwest sectors of the Norwegian coastline, RSL fell to a lowstand in the early Holocene, followed by a spatially-variable mid-Holocene Tapes transgression and a slow RSL fall to the present. The magnitude of Holocene lowstands and transgressions vary by location and distance from formerly glaciated areas. In

southwest Norway, an additional coastal RSL transgression occurred during the YD stadial. We produce spatiotemporally continuous maps of Tapes and YD transgression amplitudes and timings, and conclude from them that locations that record Tapes transgression maxima were influenced primarily by competition between GMSL rise and isostatic uplift, with additional possible influence in the late Holocene by peripheral bulge migration.

The standardized database presented here provides a high-quality constraint to test GIA models in order to refine existing ice histories such as ICE-6G, GLAC-1D (Abe-Ouchi et al., 2015; Tarasov et al., 2012; Tarasov and Richard Peltier, 2002; Briggs et al., 2014), UIT (Patton et al., 2017), N05 (Näslund et al., 1994), and ANU (Lambeck et al., 2010); to produce new ice histories; and to further constrain Norwegian solid earth structure. Updating ice and Earth models could be performed in a variety of ways, for instance by combining our STEHME results with an adjoint inversion approach (Crawford et al., 2018). Lastly, our work demonstrates that existing data in the northern half of Norway—especially Svartisen, Salten, Helgeland, Finnmark, and the Lofoten-Vesterålen archipelago—are insufficient to fully characterize local RSL histories and regional trends in Eurasian ice sheet melt, and cause high STEHME uncertainties in the deglacial and early Holocene (Figs. 9B, 13 and 11 ka). Our data compilation and spatiotemporal modeling provides an important step towards better constraining EIS history and Norwegian Earth structure.

Data availability

Datasets and model outputs zenodo.comrelated to this article can be found online at https://doi.org/10.5281/zenodo.6330206 on Zenodo, an open science and open data repository. Datasets include the HOLSEA database produced in this article (also available in supplementary material) as well as the mean and standard deviation of the STEHME.

Author contributions

RC and JA conceived and designed the research; RC, WD, and NB compiled data with additional guidance from NK; RC wrote and executed the STEHME code with guidance on model design from EA and BD and on statistics from WM; RC used the GIA model by JA to generate the GIA prior; RC drafted figures and wrote the original draft with help from JA; all authors contributed to manuscript review and editing.

Declaration of competing interest

The authors declare that they have no known competing financial interests or personal relationships that could have appeared to influence the work reported in this paper.

Acknowledgements

Appendix A. Supplementary data

Supplementary data to this article can be found online at https://doi.org/10.1016/j.quascirev.2022.107422.

References

Abe-Ouchi, A., Saito, F., Kageyama, M., Braconnot, P., Harrison, S.P., Lambeck, K., Otto-Bleisner, B., Peltier, W.R., Tarasov, L., Peterschmitt, J.Y., Takahashi, K., 2015. Ice-sheet configuration in the CMIP5/PMIP3 last glacial maximum experiments. Geosci. Model Dev. (GMD) 8, 3621–3637.

Andersen, B.G., 1960. Sørlandet I Sen- Og Postglacial Tid (English Summary). Norges geologiske undersøkelse., pp. 1–142

Andersen, B.G., 1968. Glacial Geology of Western Troms, North Norway. *Norges geologiske undersøkelse*, p. 165.

Anundsen, K., 1978. Marine transgression in younger Dryas in Norway. Boreas 7 (1), 49–60.

Anundsen, K., 1985. Changes in shore-level and ice-front position in Late Weichsel and Holocene, southern Norway. Norsk Geografisk Tidsskrift - Norwegian Journal of Geography 39 (4), 204–225.

Anundsen, K., Fjeldskaar, W., 1983. Observed and Theoretical Late Weichselian Shore-Level Changes Related to Glacier Oscillations at Yrkje, South-West Norway. Late- and postglacial oscillations of glaciers: glacial and periglacial forms. Colloquium, Trier, pp. 133–170, 1980.

Argus, D.F., Peltier, W.R., Drummond, R., Moore, A.W., 2014. The Antarctica component of postglacial rebound model ICE-6G_c (VM5a) based on GPS positioning, exposure age dating of ice thicknesses, and relative sea level histories. Geophys. J. Int. 198, 537–563.

Artemieva, I.M., 2019. Lithosphere structure in Europe from thermal isostasy. Earth Sci. Rev. 188, 454–468.

Arvidsson, R., 1996. Fennoscandian earthquakes: whole crustal rupturing related to postglacial rebound. Science 274 (5288), 744–746 (Publisher: American Association for the Advancement of Science Section: Reports).

Ashe, E.L., Cahill, N., Hay, C., Khan, N.S., Kemp, A., Engelhart, S.E., Horton, B.P., Parnell, A.C., Kopp, R.E., 2019. Statistical modeling of rates and trends in Holocene relative sea level. Quat. Sci. Rev. 204, 58–77.

Auriac, A., Whitehouse, P.L., Bentley, M.J., Patton, H., Lloyd, J.M., Hubbard, A., 2016. Glacial isostatic adjustment associated with the Barents Sea ice sheet: a modelling inter-comparison. Quat. Sci. Rev. 147, 122–135.

Austad, R., Erichsen, C., 1987. Strandforskyvning På Nord-Karmøy Basert På Pollen- Og Diatomeanalyse. Ph.D. thesis. University of Bergen. Accepted: 2017-11-06T09:48:28Z Publisher: The University of Bergen.

Austermann, J., Mitrovica, J.X., Latychev, K., Milne, G.A., 2013. Barbados-based estimate of ice volume at Last Glacial Maximum affected by subducted plate. Nat. Geosci. 6 (7), 553–557. Number: 7 Publisher: Nature Publishing Group.

Authority, N.M., 2021. Tide Tables for the Norwegian Coast Including Svalbard and Dover, England. Tech. rep.. Norwegian Mapping Authority, Stavanger.

Baggenstos, D., Häberli, M., Schmitt, J., Shackleton, S.A., Birner, B., Severinghaus, J.P., Kellerhals, T., Fischer, H., 2019. Earth's radiative imbalance from the Last Glacial Maximum to the present, 30. In: Proceedings of the National Academy of Sciences, vol. 116. Publisher: National Academy of Sciences Section: Physical Sciences, ISBN 9781905447114, pp. 14881–14886.

Bakke, J., Dahl, S.O., Paasche, Ø., Løvlie, R., Nesje, A., 2005. Glacier fluctuations, equilibrium-line altitudes and palaeoclimate in Lyngen, northern Norway, during the Lateglacial and Holocene. Holocene 15 (4), 518–540 (Publisher: SAGE Publications Ltd).

Balascio, N.L., Zhang, Z., Bradley, R.S., Perren, B., Dahl, S.O., Bakke, J., 2011. A multi-proxy approach to assessing isolation basin stratigraphy from the Lofoten Islands, Norway. Quat. Res. 75 (1), 288–300.

Bang-Andersen, S., 1995. Mesolithic Man and the Rising Sea Spotlighted by Three Tapes-Transgressed Sites in SW Norway. Oxbow books, 113-121, Accepted: 2013-03-13T11:36:17Z Publisher.

Bang-Andersen, S., 2003. Southwest Norway at the pleistocene/holocene transition: landscape development, colonization, site types, settlement patterns. Norweg. Archaeol. Rev. 36 (1), 5–25. https://doi.org/10.1080/00293650307293. Publisher: Routledge _eprint:

Baranskaya, A.V., Khan, N.S., Romanenko, F.A., Roy, K., Peltier, W.R., Horton, B.P., 2018. A postglacial relative sea-level database for the Russian Arctic coast. Quat. Sci. Rev. 199, 188–205.

Barnett, R.L., Gehrels, W.R., Charman, D.J., Saher, M.H., Marshall, W.A., 2015. Late Holocene sea-level change in arctic Norway. Quat. Sci. Rev. 107, 214–230.

Barnhardt, W.A., Roland Gehrels, W., Kelley, J.T., 1995. Late Quaternary relative sea-level change in the western Gulf of Maine: evidence for a migrating glacial forebulge. Geology 23 (4), 317–320.

Barnhoorn, A., Wal, W.v.d., Vermeersen, B.L.A., Drury, M.R., 2011. Lateral, radial, and temporal variations in upper mantle viscosity and rheology under Scandinavia. G-cubed 12 (1).

Batterson, M.J., Newfoundland and Labrador, & Geological Survey, 2003. Quaternary Geography and Sedimentology of the Humber River Basin and Adjacent Areas. Govt. of Newfoundland and Labrador, Geological Survey, St. John's, OCLC: 54905684.

Bell, T., 1996. The last glaciation and sea level history of Fosheim peninsula, ellesmere island, Canadian high arctic. Can. J. Earth Sci. 33 (7), 1075–1086.

Billah, M., 2020. Holocene Relative Sea-Level Changes in Evenes, Northern Norway, p. 107.

Bird, E., Klemsdal, T., 1986. Shore displacement and the origin of the lagoon at Brusand, southwestern Norway. Norsk Geografisk Tidsskrift-norwegian Journal of Geography – NORSK GEOGR TIDSSKR-NOR J GEO 40, 27–35.

Bondevik, S., Mangerud, J., 2002. A calendar age estimate of a very late Younger Dryas ice sheet maximum in western Norway. Quat. Sci. Rev. 21 (14), 1661–1676.

Bondevik, S., Svendsen, J.I., Johnsen, G., Mangerud, J., Kaland, P.E., 1997a. The Storegga tsunami along the Norwegian coast, its age and run up. Boreas 26 (1), 29–53. _eprint: https://onlinelibrary.wiley.com/doi/pdf/10.1111/j.1502-3885.1997.tb00649.x.

Bondevik, S., Svendsen, J.I., Mangerud, J., 1997b. Tsunami sedimentary facies deposited by the Storegga tsunami in shallow marine basins and coastal lakes, western Norway. Sedimentology 44 (6), 1115–1131. _eprint: https://onlinelibrary.wiley.com/doi/pdf/10.1046/j.1365-3091.1997.d01-63.x.

Bondevik, S., Svendsen, J.I., Mangerud, J., 1998. Distinction between the Storegga tsunami and the holocene marine transgression in coastal basin deposits of western Norway. J. Quat. Sci. 13 (6), 529–537.

Bondevik, S., Mangerud, J., Birks, H.H., Gulliksen, S., Reimer, P., 2006. Changes in north atlantic radiocarbon reservoir ages during the Allerød and younger Dryas. Science 312 (5779), 1514–1517 (Publisher: American Association for the Advancement of Science Section: Report).

Bondevik, S., Stormo, S.K., Skjerdal, G., 2012. Green mosses date the Storegga tsunami to the chilliest decades of the 8.2 ka cold event. Quat. Sci. Rev. 45, 1–6.

Bondevik, S., Lødøen, T.K., Tøssebro, C., Årskog, H., Hjelle, K.L., Mehl, I.K., 2019. Between winter storm surges – human occupation on a growing Mid-Holocene transgression maximum (Tapes) beach ridge at Longva, Western Norway. Quat. Sci. Rev. 215, 116–131.

Bradley, S.L., Milne, G.A., Horton, B.P., Zong, Y., 2016. Modelling sea level data from China and Malay-Thailand to estimate Holocene ice-volume equivalent sea level change. Quat. Sci. Rev. 137, 54–68.

Brendryen, J., Haflidason, H., Yokoyama, Y., Haaga, K.A., Hannisdal, B., 2020. Eurasian Ice Sheet collapse was a major source of Meltwater Pulse 1A 14,600 years ago. Nat. Geosci. 13 (5), 363–368. Number: 5 Publisher: Nature Publishing Group.

Briggs, R.D., Pollard, D., Tarasov, L., 2014. A data-constrained large ensemble analysis of Antarctic evolution since the Eemian. Quat. Sci. Rev. 103, 91–115.

Carrere, L., Lyard, F., Cancet, M., Guillot, A., 2015. FES 2014, a new tidal model on the global ocean with enhanced accuracy in shallow seas and in the Arctic region. EGU general assembly 17, 5481.

Celsius, A., 1743. Anmärkning Om Vatnets Förminskande S\aa I Östersiön Som Vesterhafvet, vol. 4. Kongl. Swenska Wetenskaps Academiens Handlingar, Stockholm.

Corner, G.D., Haugane, E., 1993. Marine-lacustrine stratigraphy of raised coastal basins and postglacial sea-level change at Lyngen and Vanna, Troms, northern Norway. Nor. Geol. Tidsskr. 73 (3), 175–197.

Corner, G.D., Yevzerov, V.Y., Kolka, V.V., Møller, J.J., 1999. Isolation basin stratigraphy and Holocene relative sea-level change at the Norwegian—Russian border north of Nikel, northwest Russia. Boreas 28 (1), 146–166.

Costa, S., 2018. IOSACal: v0.4.0.

Crawford, O., Al-Attar, D., Tromp, J., Mitrovica, J.X., Austermann, J., Lau, H.C.P., 2018. Quantifying the sensitivity of post-glacial sea level change to laterally varying viscosity. Geophys. J. Int. 214 (2), 1324–1363.

Cressie, N., Wikle, C.K., 2015. Statistics for Spatio-Temporal Data. John Wiley & Sons. Google-Books-ID: 4L_dCgAAQBAJ.

Dangendorf, S., Hay, C., Calafat, F.M., Marcos, M., Piecuch, C.G., Berk, K., Jensen, J., 2019. Persistent acceleration in global sea-level rise since the 1960s. Nat. Clim. Change 9 (9), 705–710.

Davis, P.T., Menounos, B., Osborn, G., 2009. Holocene and latest Pleistocene alpine glacier fluctuations: a global perspective. Quat. Sci. Rev. 28 (21), 2021–2033.

Dawson, A., Bondevik, S., Teller, J., 2011. Relative timing of the Storegga submarine slide, methane release, and climate change during the 8.2 ka cold event. Holocene 21 (7), 1167–1171 (Publisher: SAGE Publications Ltd).

De Geer, G., 1888. Om Skandinaviens nivåförändringar under qvartärperioden. Geol. Foren. Stockh. Forh. 10 (5), 366–379.

Donner, J., Eronen, M., Jungner, H., 1977. The dating of the Holocene relative sea-level changes in Finnmark, North Norway. Norsk Geografisk Tidsskrift - Norwegian Journal of Geography 31 (3), 103–128.

Dyke, A.S., Peltier, W.R., 2000. Forms, response times and variability of relative sea-level curves, glaciated North America. Geomorphology 32 (3), 315–333.

Dziewonski, A.M., Anderson, D.L., 1981. Preliminary reference Earth model. Phys. Earth Planet. In. 25 (4), 297–356.

Ekman, M., 1991. A concise history of postglacial land uplift research (from its beginning to 1950). Terra. Nova 3 (4), 358–365. _eprint: https://onlinelibrary.wiley.com/doi/pdf/10.1111/j.1365-3121.1991.tb00163.x.

Engelhart, S.E., Vacchi, M., Horton, B.P., Nelson, A.R., Kopp, R.E., 2015. A sea-level database for the Pacific coast of central North America. Quat. Sci. Rev. 113, 78–92.

England, J., 1992. Postglacial emergence in the Canadian High Arctic: integrating glacioisostasy, eustasy, and late deglaciation. Can. J. Earth Sci. 29 (5), 984–999 (Publisher: GeoScienceWorld).

Faleide, J.I., Tsikalas, F., Breivik, A., Mjelde, R., Ritzmann, O., Engen, O., Wilson, J., Eldholm, O., 2008. Structure and evolution of the continental margin off Norway and the Barents Sea. Episodes 31, 82–91.

Farrell, W.E., Clark, J.A., 1976. On postglacial sea level. Geophys. J. Roy. Astron. Soc.

46 (3), 647–667.

Fægri, K., 1944. On the introduction of agriculture in western Norway. Geol. Foren. Stockh. Forh. 66 (3), 449–462. https://doi.org/10.1080/11035894409445688. Publisher: Taylor & Francis _eprint.

Fægri, K., 1954. On the peri-glacial flora of jæren. With notes on the morphology of the salix pollen grain. Norsk Geografisk Tidsskrift - Norwegian Journal of Geography 14 (1–4), 61–76. https://doi.org/10.1080/00291955308542716. Publisher: Routledge _eprint.

Fjeldskaar, W., Amantov, A., 2018. Younger Dryas transgression in western Norway: a modelling approach. Norw. J. Geol. 98.

Fjeldskaar, W., Bondevik, S., 2020. The Early-Mid Holocene transgression (Tapes) at the Norwegian coast – comparing observations with numerical modelling. Quat. Sci. Rev. 242, 106435.

Fletcher, C.H., Fairbridge, R.W., Moller, J.J., Long, A.J., 1993. Emergence of the varanger peninsula, arctic Norway, and climate changes since deglaciation. Holocene 3 (2), 116–127 (Publisher: SAGE Publications Ltd).

Fodnes, N.I., 1996. Strandforskyvning i indre Laksefjord, Finnmark - belyst ved sedimentologi og diatomkanalyse av borekjerner fra isolasjonsbassenger. University of Bergen. Unpublished cand. scient. thesiis.

Gabrielsen, G., 1959. A marine transgression of boreal age in the southernmost part of Norway. Nature 183 (4675), 1616–1617. Number: 4675 Publisher: Nature Publishing Group.

Gaffney, V., Fitch, S., Bates, M., Ware, R.L., Kinnaird, T., Gearey, B., Hill, T., Telford, R., Batt, C., Stern, B., Whittaker, J., Davies, S., Sharada, M.B., Everett, R., Cribdon, R., Kistler, L., Harris, S., Kearney, K., Walker, J., Muru, M., Hamilton, D., Law, M., Bates, R., Allaby, R.G., 2020. Multi-proxy Evidence for the Impact of the Storegga Slide Tsunami on the Early Holocene Landscapes of the Southern North Sea bioRxiv, p. 2020.02.24.962605.

García-Artola, A., Stéphan, P., Cearreta, A., Kopp, R.E., Khan, N.S., Horton, B.P., 2018. Holocene sea-level database from the Atlantic coast of Europe. Quat. Sci. Rev. 196, 177–192.

Gehrels, W.R., Long, A.J., 2007. Quaternary land–ocean interactions: sea-level change, sediments and tsunami. Mar. Geol. 1–3 (242), 1–4.

Glørstad, H., 2016. Deglaciation, sea-level change and the Holocene colonization of Norway. Geological Society, London, Special Publications 411 (1), 9–25.

Grande, R.C., Walsh, T.J., Chowdhary, G., Ferguson, S., How, J.P., 2016. Online regression for data with changepoints using Gaussian processes and reusable models. IEEE Transact. Neural Networks Learn. Syst. 1–14.

Greenwood, S.L., Simkins, L.M., Halberstadt, A.R.W., Prothro, L.O., Anderson, J.B., 2018. Holocene reconfiguration and readvance of the east antarctic ice sheet. Nat. Commun. 9 (1), 3176.

Griffiths, S.D., Hill, D.F., 2015. Tidal modeling. In: Handbook of Sea-Level Research. John Wiley & Sons, Ltd, pp. 438–451.

Griffiths, S.D., Peltier, W.R., 2009. Modeling of polar ocean tides at the last glacial maximum: amplification, sensitivity, and climatological implications. J. Clim. 22 (11), 2905–2924.

Grothaug Andersen, B., 1975. Glacial Geology of Northern Nordland, North Norway. Univ.-Forl., Trondheim [u.a., p. 247679608. OCLC.

Gulliksen, S., Nydal, R., Lövseth, K., 1975. Trondheim natural radiocarbon measurements VII. Radiocarbon 17 (3), 364–395 (Publisher: Cambridge University Press).

Gulliksen, S., Nydal, R., Skogseth, F., 1978. Trondheim natural radiocarbon measurements VIII. Radiocarbon 20 (1), 105–133 (Publisher: Cambridge University Press).

Hafsten, U., 1960. Pollen-analytic investigations in South Norway. Vegetation, climate, shore-line displacement, land occupation. Norges geologiske undersøkelse 208, 434–462.

Hafsten, U., 1983. Shore-level changes in South Norway during the last 13,000 years, traced by biostratigraphical methods and radiometric datings. Norsk Geografisk Tidsskrift - Norwegian Journal of Geography 37 (2), 63–79.

Hafsten, U., Tallantire, P.A., 1978. Palaeoecology and post-Weichselian shore-level changes on the coast of Møre, western Norway. Boreas 7 (2), 109–122. _eprint: https://onlinelibrary.wiley.com/doi/pdf/10.1111/j.1502-3885.1978.tb00269.x.

Hald, M., Vorren, T.O., 1983. A shore displacement curve from the Tromsø district, North Norway. Nor. Geol. Tidsskr. 63 (2–3), 103–110.

Hay, C.C., Lau, H.C.P., Gomez, N., Austermann, J., Powell, E., Mitrovica, J.X., Latychev, K., Wiens, D.A., 2017. sea level fingerprints in a region of complex earth structure: the case of WAIS. J. Clim. 30 (6), 1881–1892.

Heaton, T.J., Köhler, P., Butzin, M., Bard, E., Reimer, R.W., Austin, W.E.N., Ramsey, C.B., Grootes, P.M., Hughen, K.A., Kromer, B., Reimer, P.J., Adkins, J., Burke, A., Cook, M.S., Olsen, J., Skinner, L.C., 2020. MARINE20—the marine radiocarbon age calibration curve (0–55,000 cal BP). Radiocarbon 1–42 (Publisher: Cambridge University Press).

Helle, S.K., 2006. Early Post-deglaciation Shorelines and Sea-Level Changes along Hardangerfjorden and Adjacent Fjord Areas, W. Norway. Ph.D. thesis. University of Bergen, Bergen. Publisher: The University of Bergen).

Helle, S.K., Anundsen, K., Aasheim, S., Haflidason, H., 1997. Indications of a younger Dryas marine transgression in inner hardanger, west Norway. Nor. Geol. Tidsskr. 77, 101–117.

Helle, S.K., Rye, N., Stabell, B., Prösch-Danielsen, L., Hoel, C., 2007. Neotectonic faulting and the Late Weichselian shoreline gradients in SW Norway. J. Geodyn. 44 (3), 96–128.

Helskog, K., 1978. Late Holocene sea-level changes seen from prehistoric settlements. Norsk Geografisk Tidsskrift - Norwegian Journal of Geography 32 (3), 111–119. https://doi.org/10.1080/00291957808552032. Publisher: Routledge

_eprint:

Hendy, C.H., Hall, B.L., 2006. The radiocarbon reservoir effect in proglacial lakes: examples from Antarctica. Earth Planet Sci. Lett. 241 (3), 413–421.

Henningsmoen, K., 1978. En karbon-datest strandforskyvings curve fra søndre Vesfold, *Fortiden i Søkelyset, Laboratoiriet for Radiologisk Datering*, pp. 239–247. Oslo, Hydal, R., Westin, S., Hafsten, U. & Gulliksen, S.

Høgestøl, M., Prøsch-Danielsen, L., Walderhaug, O., 2019. Bergkunst På Midt- Og Sør-Jæren Samt I Dalaneregionen, Rogaland. Motiver, Historikk, Naturmiljø Og Tilstand, pp. 1–83. AmS-Varia.

Hijma, M.P., Engelhart, S.E., Törnqvist, T.E., Horton, B.P., Hu, P., Hill, D.F., 2015. A protocol for a geological sea-level database. In: Handbook of Sea-Level Research. John Wiley & Sons, Ltd, pp. 536–553.

Håkansson, S., 1969. University of Lund radiocarbon dates II. Radiocarbon 11 (2), 430–450 (Publisher: Cambridge University Press).

Hoeg, H., 1995. Pollenanalyse - Lista., Farsundprosjektet : Stenalderbopladser På Lista, pp. 268–323.

Hu, P., 2010. Developing a Quality-Controlled Postglacial Sea-Level Database For Coastal Louisiana to Assess Conflicting Hypotheses Of Gulf Coast Sea-Level Change. Master's thesis. Tulane University, New Orleans.

Huang, P., Wu, P., Steffen, H., 2019. In search of an ice history that is consistent with composite rheology in Glacial Isostatic Adjustment modelling. Earth Planet Sci. Lett. 517, 26–37.

Hughes, A.L.C., Gyllencreutz, R., Lohne, Ø.S., Mangerud, J., Svendsen, J.I., 2016. The last Eurasian ice sheets – a chronological database and time-slice reconstruction, DATED-1. Boreas 45 (1), 1–45.

Hyvärinen, H., 1975. Absolute and relative pollen diagrams from northernmost Fennoscandia. Fennia - International Journal of Geography 142 (1). Number: 1.

Johansen, I., 1985. Deglasiasjonsforløpet på Tingvollhalvøya og tilgrensende områder, Nordvestlandet, i lys av vegetasjonsutviklingen. Norsk Geografisk Tidsskrift - Norwegian Journal of Geography 39 (3), 155–174.

Johnsen, I.S., 2017. Strandforskyvning På Bokn Og Deglasiasjonen Av Boknafjorden, Rogaland. Master's thesis. University of Bergen, Bergen. Accepted: 2017-08-04T07:49:06Z Publisher: The University of Bergen.

Jordan, J.W., 2001. Late quaternary sea level change in southern beringia: postglacial emergence of the western Alaska peninsula. Quat. Sci. Rev. 20 (1), 509–523.

Juhl, K., 2001. *Austbø På Hundvåg Gennem 10 000 År : Arkæologiske Undersøgelser I Stavanger Kommune 1987–1990, Rogaland, Syd-Vest Norge*, Stavanger : Arkeologisk Museum I Stavanger. Accepted: 2014-09-02T12:57:25Z ISSN: 0332–6306.

Jungren, H., Sonninen, E., 1989. Radiocarbon Dates III. Dating Laboratory at the University of Helsinki.

Kachuck, S.B., Cathles, L.M., 2018. Constraining the geometry and volume of the Barents Sea ice sheet. J. Quat. Sci. 33 (5), 527–535. _eprint: https://onlinelibrary.wiley.com/doi/pdf/10.1002/jqs.3031.

Kaland, P.E., 1984. Holocene shore displacement and shorelines in Hordaland, western Norway. Boreas 13 (2), 203–242. _eprint: https://onlinelibrary.wiley.com/doi/pdf/10.1111/j.1502-3885.1984.tb00070.x.

Kaland, T., 1988. Strandforskyvning I Hjelmeland, Ryfylke. Bio- Og Litostratigrafiske Bassengundersøkelser På Randøy Og Ved Fister. Master's thesis. University of Bergen, Bergen. Accepted: 2017-10-20T09:23:53Z Publisher: The University of Bergen.

Karlsen, L.C., 2009. Lateglacial vegetation and environment at the mouth of Hardangerfjorden, western Norway. Boreas 38 (2), 315–334. _eprint: https://onlinelibrary.wiley.com/doi/pdf/10.1111/j.1502-3885.2008.00062.x.

Kelsey, H.M., Witter, R.C., Engelhart, S.E., Briggs, R., Nelson, A., Haeussler, P., Corbett, D., 2015. Beach ridges as paleoseismic indicators of abrupt coastal subsidence during subduction zone earthquakes, and implications for Alaska-Aleutian subduction zone paleoseismology, southeast coast of the Kenai Peninsula, Alaska. Quat. Sci. Rev. 113, 147–158.

Kendall, R.A., Mitrovica, J.X., Milne, G.A., 2005. On post-glacial sea level - II. Numerical formulation and comparative results on spherically symmetric models. Geophys. J. Int. 161 (3), 679–706. WOS:000229792700009.

Khan, N.S., Ashe, E., Horton, B.P., Dutton, A., Kopp, R.E., Brocard, G., Engelhart, S.E., Hill, D.F., Peltier, W.R., Vane, C.H., Scatena, F.N., 2017. Drivers of Holocene sea-level change in the caribbean. Quat. Sci. Rev. 155, 13–36.

Khan, N.S., Horton, B.P., Engelhart, S., Rovere, A., Vacchi, M., Ashe, E.L., Törnqvist, T.E., Dutton, A., Hijma, M.P., Shennan, I., 2019. Inception of a global atlas of sea levels since the Last Glacial Maximum. Quat. Sci. Rev. 220, 359–371.

Kingslake, J., Scherer, R.P., Albrecht, T., Coenen, J., Powell, R.D., Reese, R., Stansell, N.D., Tulaczyk, S., Wearing, M.G., Whitehouse, P.L., 2018. Extensive retreat and re-advance of the West Antarctic ice sheet during the holocene. Nature 558 (7710), 430.

Kjemperud, A., 1981a. Diatom changes in sediments of basins possessing marine/lacustrine transitions in Frosta, Nord-Trøndelag, Norway. Boreas 10 (1), 27–38. _eprint: https://onlinelibrary.wiley.com/doi/pdf/10.1111/j.1502-3885.1981.tb00466.x.

Kjemperud, A., 1981b. A shoreline displacement investigation from frosta in trondheimsfjorden, nord-trondelag, Norway. NOR. GEOL. TIDSSKR. 61 (1), 1–15. Num Pages: 15.

Kjemperud, A., 1986. Late weichselian and holocene shoreline displacement in the Trondheimsfjord area, central Norway. Boreas 15 (1), 61–82.

Knies, J., Vogt, C., Matthiessen, J., Nam, S.-I., Ottesen, D., Rise, L., Bargel, T., Eilertsen, R.S., 2007. Re-advance of the fennoscandian ice sheet during heinrich event 1. Mar. Geol. 240 (1), 1–18.

Kopp, R.E., Kemp, A.C., Bittermann, K., Horton, B.P., Donnelly, J.P., Gehrels, W.R.,

Hay, C.C., Mitrovica, J.X., Morrow, E.D., Rahmstorf, S., 2016. Temperature-driven global sea-level variability in the Common Era. Proc. Natl. Acad. Sci. Unit. States Am. 113 (11), E1434–E1441.

Koshechkin, 1975. Relocation of the Coastliine of the Barents Sea and White Sea in Late Deglacial Time (In Russian). Izvestia of the Academy of Sciences of the USSR Geographic series, p. 10.

Krzywinski, K., Stabell, B., 1984. Late Weichselian sea level changes at Sotra, Hordaland, western Norway. Boreas 13 (2), 159–202.

Kui, T.W., 1996. Stransforskyvning i indre Laksefjord, Finnmark. Belyst ved analyser av pollen og alger fra borkjerner. Ph.D. thesis. University of Bergen.

Lagerbäck, R., Sundh, M., 2008. *Early Holocene faulting and paleoseismicity in northern Sweden*, no. 836. In: Serie C, Avhandlingar Och Uppsatser. Sveriges Geologiska Undersökning. Uppsala, OCLC: 313989533.

Lambeck, K., Smither, C., Johnston, P., 1998. Sea-level change, glacial rebound and mantle viscosity for northern Europe. Geophys. J. Int. 134 (1), 102–144.

Lambeck, K., Purcell, A., Funder, S., KJæR, K.H., Larsen, E., Moller, P., 2006. Constraints on the Late Saalian to early Middle Weichselian ice sheet of Eurasia from field data and rebound modelling. Boreas 35 (3), 539–575. _eprint: https://onlinelibrary.wiley.com/doi/pdf/10.1080/03009480600781875.

Lambeck, K., Purcell, A., Zhao, J., Svensson, N.-O., 2010. The scandinavian ice sheet: from MIS 4 to the end of the last glacial maximum. Boreas 39 (2), 410–435. _eprint: https://onlinelibrary.wiley.com/doi/pdf/10.1111/j.1502-3885.2010. 00140.x.

Lambeck, K., Rouby, H., Purcell, A., Sun, Y., Sambridge, M., 2014. sea level and global ice volumes from the last glacial maximum to the holocene. Proc. Natl. Acad. Sci. Unit. States Am. 111 (43), 15296–15303.

Lei, W., Ruan, Y., Bozdağ, E., Peter, D., Lefebvre, M., Komatitsch, D., Tromp, J., Hill, J., Podhorszki, N., Pugmire, D., 2020. Global adjoint tomography—model GLADM25. Geophys. J. Int. 223 (1), 1–21.

Lid, K.A., 2019. Holocen Strandforskyvning Ved Skånland, Troms/Holocene Shore Displacement at Skånland, Troms, Northern Norway. Master's thesis. University of Bergen, Bergen. Accepted: 2020-01-22T03:40:07Z Publisher: The University of Bergen.

Lie, S.E., Stabell, B., Mangerud, J., 1983. Diatom stratigraphy related to Late Weichselian sea-level changes in Sunnmøre, western Norway. Norges geologiske undersøkelse 380, 203–219.

Lin, Y., Hibbert, F.D., Whitehouse, P.L., Woodroffe, S.A., Purcell, A., Shennan, I., Bradley, S.L., 2021. A reconciled solution of Meltwater Pulse 1A sources using sea-level fingerprinting. Nat. Commun. 12 (1), 2015. Number: 1 Publisher: Nature Publishing Group.

Lindblom, I., Simonsen, A., Solheim, H., 1997. Husøy - Palaeoecology and Prehistory of a Small Island on the SW Coast of Norway., Husøy : Palaeoecology and Prehistory of a Small Island on the SW Coast of Norway/, pp. 0–38.

Lise Kristiansen, I., Mangerud, J., Lømo, L., 1988. Late weichselian/early holocene pollen-and lithostratigraphy in lakes in the ålesund area, western Norway. Rev. Palaeobot. Palynol. 53 (3), 185–231.

Liu, J., Milne, G.A., Kopp, R.E., Clark, P.U., Shennan, I., 2016. Sea-level constraints on the amplitude and source distribution of Meltwater Pulse 1A. Nat. Geosci. 9 (2), 130–134. Number: 2 Publisher: Nature Publishing Group.

Lloyd, J., 2000. Combined foraminiferal and Theocamoebian environmental reconstructioon from an issolation basin in NW Scotland: implications for sealevel studies. J. Foraminifer. Res. 30 (4), 294–305.

Lohne, Ø.S., 2006. Late Weichselian Relative Sea-Level Changes and Glacial History in Hordaland, Western Norway. The University of Bergen. Accepted: 2006-05-10T13:32:47Z.

Lohne, Ø.S., Bondevik, S., Mangerud, J., Schrader, H., 2004. Calendar year age estimates of Allerød–Younger Dryas sea-level oscillations at Os, western Norway. J. Quat. Sci. 19 (5), 443–464. _eprint: https://onlinelibrary.wiley.com/doi/pdf/ 10.1002/jqs.846.

Lohne, Ø.S., Bondevik, S., Mangerud, J., Svendsen, J.I., 2007. Sea-level fluctuations imply that the Younger Dryas ice-sheet expansion in western Norway commenced during the Allerød. Quat. Sci. Rev. 26 (17), 2128–2151.

Long, A.J., Woodroffe, S.A., Roberts, D.H., Dawson, S., 2011. Isolation basins, sea-level changes and the Holocene history of the Greenland Ice Sheet. Quat. Sci. Rev. 30 (27), 3748–3768.

Mangerud, J., Aarseth, I., Hughes, A.L.C., Lohne, Ø.S., Skår, K., Sønstegaard, E., Svendsen, J.I., 2016. A major re-growth of the scandinavian ice sheet in western Norway during allerød-younger Dryas. Quat. Sci. Rev. 132, 175–205.

Marthinussen, M., 1960. Coast-and Fjord Area of Finnmark. With Remarks on Other Districts. Norges Geologiske Undersøkelse, pp. 416–434.

Marthinussen, M., 1962. 14C-datings referring to shore lines, transgressions, and glacial substages in Northern Norway. Norges geologiske undersøkelse 215, 37–67.

Marthinussen, M., 1974. Contributions to the Quaternary geology of northeasternmost Norway and the closely adjoining foreign territories. Norges geologiske undersøkelse 28 (315), 100–140, 25–44.

Matthews, A.G.d.G., van der Wilk, M., Nickson, T., Fujii, K., Boukouvalas, A., León-Villagrá, P., Ghahramani, Z., Hensman, J., 2016. GPflow: A Gaussian Process Library Using TensorFlow. *arXiv:1610.08733 [stat]*, arXiv: 1610.08733.

Mchutchon, A., Rasmussen, C.E., 2011. Gaussian process training with input noise. In: Shawe-Taylor, J., Zemel, R.S., Bartlett, P.L., Pereira, F., Weinberger, K.Q. (Eds.), Advances in Neural Information Processing Systems 24. Curran Associates, Inc, pp. 1341–1349.

McManus, J.F., Francois, R., Gherardi, J.-M., Keigwin, L.D., Brown-Leger, S., 2004. Collapse and rapid resumption of Atlantic meridional circulation linked to deglacial climate changes. Nature 428 (6985), 834–837. Number: 6985 Publisher: Nature Publishing Group.

Menke, W., 2018. Geophysical Data Analysis: Discrete Inverse Theory. Academic Press. Google-Books-ID: OG89DwAAQBAJ.

Midtbø, I., Skjelstad, G., Nyland, A.J., Olsen, T.B., Tellefsen, M., 2011. Steinalderboplasser På Fosenhalvøya : Arkeologiske Og Naturvitenskapelige Undersøkelser 2004-2007 T-Forbindelsen, Karmøy Kommune, Nord-Rogaland. Skjelstad, G., Midtbø, I., Nyland, A.J., Olsen, T.B og Tellefsen, M. (2011) Steinalderboplasser på Fosenhalvøya : arkeologiske og naturvitenskapelige undersøkelser 2004-2007 T-forbindelsen, Karmøy kommune, Nord-Rogaland. Stavanger : Arkeologisk museum i Stavanger, Accepted: 2015-02-05T12:12:06Z ISSN: 0332-6306 Publication Title: 267.

Midtun, E.S., 2019. Holosen Strandforskyvning for Leknes, Vestvågøy. Master's thesis. University of Bergen, Bergen. Accepted: 2019-10-02T11:42:36Z Publisher: The University of Bergen.

Mienert, J., Vanneste, M., Haflidason, H., Bünz, S., 2010. Norwegian margin outer shelf cracking: a consequence of climate-induced gas hydrate dissociation? Int. J. Earth Sci. 99 (1), 207–225.

Milne, G.A., Mitrovica, J.X., 1998. Postglacial sea-level change on a rotating Earth. Geophys. J. Int. 133 (1), 1–19.

Milne, G.A., Davis, J.L., Mitrovica, J.X., Scherneck, H.-G., Johansson, J.M., Vermeer, M., Koivula, H., 2001. Space-Geodetic constraints on glacial isostatic adjustment in Fennoscandia. Science 291 (5512), 2381–2385.

Mitrovica, J.X., Milne, G.A., 2002. On the origin of late Holocene sea-level highstands within equatorial ocean basins. Quat. Sci. Rev. 21, 2179–2190.

Møller, J.J., 1984. Holocene shore displacement at nappstraumen, lofoten, north Norway. Nor. Geol. Tidsskr 64, 1–5.

Møller, J.J., 1986. Holocene transgression maximum about 6000 years BP at ramså, vesterålen, north Norway. Norsk Geografisk Tidsskrift - Norwegian Journal of Geography 40 (2), 77–84. https://doi.org/10.1080/00291958608552158. Publisher: Routledge _eprint:

Møller, J.J., 1987. Shoreline relation and prehistoric settlement in northern Norway. Norsk Geografisk Tidsskrift - Norwegian Journal of Geography 41 (1), 45–60. https://doi.org/10.1080/00291958708552171. Publisher: Routledge _eprint:

Møller, J.J., 1995. Sandy beaches as records of changes in relative sea level and storm frequency. J. Coast Res. 169–172 (Publisher: Coastal Education & Research Foundation, Inc).

Nield, G.A., Whitehouse, P.L., van der Wal, W., Blank, B., O'Donnell, J.P., Stuart, G.W., 2018. The impact of lateral variations in lithospheric thickness on glacial isostatic adjustment in West Antarctica. Geophys. J. Int. 214 (2), 811–824.

Näslund, J.-O., Zale, R., Glazovskiy, A., 1994. The mid holocene transgression on alexandra land, Franz Josef land, Russia. Geogr. Ann. Phys. Geogr. 76 (1/2), 97–101 (Publisher: [Wiley, Swedish Society for Anthropology and Geography]).

Nydal, R., 1959. Trondheim natural radiocarbon measurements I. Radiocarbon 1, 76–80 (Publisher: Cambridge University Press).

Nydal, R., 1960. Trondheim natural radiocarbon measurements II. Radiocarbon 2, 82–96 (Publisher: Cambridge University Press).

Nydal, R., 1962. Trondheim natural radiocarbon measurements III. Radiocarbon 4, 160–182 (Publisher: Cambridge University Press).

Nydal, R., Løvseth, K., Skullerud, K.E., Holm, M., 1964. Trondheim natural radiocarbon measurements IV. Radiocarbon 6, 280–290 (Publisher: Cambridge University Press).

Nydal, R., Løvseth, K., Syrstad, O., 1970. Trondheim natural radiocarbon measurements V. Radiocarbon 12 (1), 205–237 (Publisher: Cambridge University Press).

Nydal, R., Gulliksen, S., Lövseth, K., 1972. Trondheim natural radiocarbon measurements VI. Radiocarbon 14 (2), 418–451 (Publisher: Cambridge University Press).

Nydal, R., Gulliksen, S., Loevseth, K., Skogseth, F., 1985. Trondheim natural radiocarbon measurements IX. Radiocarbon 27 (3), 525–609. Number: 3.

Olesen, O., Bungum, H., Dehls, J., Lindholm, C., Pascal, C., Roberts, D., 2013. Neotectonics, Seismicity and Contemporary Stress Field in Norway — Mechanisms and Implications, vol. 13. Geological Survey of Norway Special Publication, pp. 145–174.

Olson, B., Hashmi, I., Molloy, K., Shehu, A., 2012. Basin hopping as a general and versatile optimization framework for the characterization of biological macromolecules. Advances in Artificial Intelligence 2012 e674832, Publisher: Hindawi.

Padgett, J.S., Engelhart, S.E., Hoffmann, G., Rosentau, A., Yu, F., 2018. Sea-level change from minutes to millennia: first meeting of IGCP Project 639 in Oman. Episodes 41 (2), 5.

Patton, H., Hubbard, A., Andreassen, K., Auriac, A., Whitehouse, P.L., Stroeven, A.P., Shackleton, C., Winsborrow, M., Heyman, J., Hall, A.M., 2017. Deglaciation of the Eurasian ice sheet complex. Quat. Sci. Rev. 169, 148–172.

Peltier, W.R., Argus, D.F., Drummond, R., 2015. Space geodesy constrains ice age terminal deglaciation: the global ICE-6G_c (VM5a) model. J. Geophys. Res. Solid Earth 120 (1), 450–487.

Piecuch, C., Huybers, P., Tingley, M., 2017. Comparison of full and empirical Bayes approaches for inferring sea-level changes from tide-gauge data. J. Geophys. Res.: Oceans 122 (3), 2243–2258.

Preuss, H., 1979. Progress in computer evaluation of sea level data within the IGCP Project no. 61. In: Proc. 1978 Int. Symp. Of Coastal Evolution in the Quaternary, pp. 104–134.

Prøsch-Danielsen, L., 1993. Naturhistoriske undersokelser i rennesoy og finnoy kommuner, Rogaland, sorvest-norge. Arkeoligisk museum i Stavanger 22, 117.

Prøsch-Danielsen, L., 1996. Vegetation history and human impact during the last 11

500 years at Lista, the southernmost part of Norway. Based primarily on Professor Ulf Hafsten's material and diary from 1955–1957. Norsk Geografisk Tidsskrift - Norwegian Journal of Geography 50 (2), 85–99.

Prøsch-Danielsen, L., 1997. New light on the Holocene shore displacement curve on Lista, the southernmost part of Norway. Norsk Geografisk Tidsskrift - Norwegian Journal of Geography 51 (2), 83–101. https://doi.org/10.1080/00291959708552368. Publisher: Routledge _eprint:

Prøsch-Danielsen, L., 2006. Sea Level Studies along the Coast of of Southwestern Norway. With Emphasise on Three Short-Lived Holocene Marine Events. Arkeologisk Museum i Stavanger. Accepted: 2012-09-21T12:21:53Z Publication Title: 96.

Prøsch-Danielsen, L., Simonsen, A., 2000. The Deforestation Patterns and the Establishment of the Coastal Heathland of Southwestern Norway. Arkeologisk Museum i Stavanger. Accepted: 2012-10-04T11:59:37Z ISSN: 0800-0816.

Pétursson, H.G., Norddahl, H., Ingolfsson, O., 2015. Late Weichselian history of relative sea level changes in Iceland during a collapse and subsequent retreat of marine based ice sheet. Cuadernos de investigación geográfica/Geographical Research Letters 41 (2), 261–277 (Publisher: Universidad de La Rioja Section: Cuadernos de investigación geográfica/Geographical Research Letters).

Ramfjord, H., 1982. On the late Weichselian and Flandrian shoreline displacement in Nærøy, Nord-Trøndelag, Norway. Nor. Geol. Tidsskr 3, 191–205.

Rasmussen, A., 1981. The deglaciation of the coastal area NW of svartisen, northern Norway. Norges Geologiske Undersøkelse 369, 1–31.

Rasmussen, C.E., Williams, C.K.I., 2006. *Gaussian Processes for Machine Learning*, Adaptive Computation and Machine Learning. MIT Press, Cambridge, Mass. OCLC: ocm61285753.

Rasmussen, H., Bondevik, S., Corner, G.D., 2018. Holocene relative sea level history and Storegga tsunami run-up in Lyngen, northern Norway. J. Quat. Sci. 33 (4), 393–408. _eprint: https://onlinelibrary.wiley.com/doi/pdf/10.1002/jqs.3021.

Reimer, P.J., Austin, W.E.N., Bard, E., Bayliss, A., Blackwell, P.G., Ramsey, C.B., Butzin, M., Cheng, H., Edwards, R.L., Friedrich, M., Grootes, P.M., Guilderson, T.P., Hajdas, I., Heaton, T.J., Hogg, A.G., Hughen, K.A., Kromer, B., Manning, S.W., Muscheler, R., Palmer, J.G., Pearson, C., Plicht, J.v.d., Reimer, R.W., Richards, D.A., Scott, E.M., Southon, J.R., Turney, C.S.M., Wacker, L., Adolphi, F., Büntgen, U., Capano, M., Fahrni, S.M., Fogtmann-Schulz, A., Friedrich, R., Köhler, P., Kudsk, S., Miyake, F., Olsen, J., Reinig, F., Sakamoto, M., Sookdeo, A., Talamo, S., 2020. The IntCal20 northern hemisphere radiocarbon age calibration curve (0–55 cal kBP). Radiocarbon 62 (4), 725–757 (Publisher: Cambridge University Press).

Reite, A.J., Selnes, H., Sveian, H., Reite, 1982. A proposed deglaciation chronology for the Trondheimsfjord area , Central Norway. Norges Geologiske Undersøkelse 373, 75–84.

Rickerich, S., 2018. The Postglacial Sea Level History of Ingøya, Northern Norway. Honors Theses.

Rickers, F., Fichtner, A., Trampert, J., 2013. The Iceland–Jan Mayen plume system and its impact on mantle dynamics in the North Atlantic region: evidence from full-waveform inversion. Earth Planet Sci. Lett. 367, 39–51.

Romundset, A., Bennike, O., Bondevik, S., 2010a. Holocene Relative Sea-Level Changes and Deglaciation Chronology in Finnmark, Northern Norway. Ph.D.. UiT Munin: University of Tromsø, Tromsø.

Romundset, A., Lohne, Ø.S., Mangerud, J., Svendsen, J.I., 2010b. The first Holocene relative sea-level curve from the middle part of Hardangerfjorden, western Norway. Boreas 39 (1), 87–104.

Romundset, A., Bondevik, S., Bennike, O., 2011. Postglacial uplift and relative sea level changes in Finnmark, northern Norway. Quat. Sci. Rev. 30 (19), 2398–2421.

Romundset, A., Fredin, O., Høgaas, F., 2015. A Holocene sea-level curve and revised isobase map based on isolation basins from near the southern tip of Norway. Boreas 44 (2), 383–400.

Romundset, A., Lakeman, T.R., Høgaas, F., 2018. Quantifying variable rates of postglacial relative sea level fall from a cluster of 24 isolation basins in southern Norway. Quat. Sci. Rev. 197, 175–192.

Rosentau, A., Vassiljev, J., Saarse, L., Miidel, A., 2007. Palaeogeographic reconstruction of proglacial lakes in Estonia. Boreas 36 (2), 211–221. _eprint: https://onlinelibrary.wiley.com/doi/pdf/10.1111/j.1502-3885.2007.tb01193.x.

Rosentau, A., Klemann, V., Bennike, O., Steffen, H., Wehr, J., Latinović, M., Bagge, M., Ojala, A., Berglund, M., Becher, G.P., Schoning, K., Hansson, A., Nielsen, L., Clemmensen, L.B., Hede, M.U., Kroon, A., Pejrup, M., Sander, L., Stattegger, K., Schwarzer, K., Lampe, R., Lampe, M., Uścinowicz, S., Bitinas, A., Grudzinska, I., Vassiljev, J., Nirgi, T., Kublitskiy, Y., Subetto, D., 2021. A Holocene relative sea-level database for the Baltic Sea. Quat. Sci. Rev. 266, 107071.

Roy, K., Peltier, W.R., 2017. Space-geodetic and water level gauge constraints on continental uplift and tilting over North America: regional convergence of the ICE-6G_c (VM5a/VM6) models. Geophys. J. Int. 210 (2), 1115–1142 (Publisher: Oxford Academic).

Rundgren, M., Ingólfsson, Ó., Björck, S., Jiang, H., Haflidason, H., 1997. Dynamic sea-level change during the last deglaciation of northern Iceland. Boreas 26 (3), 201–215. _eprint: https://onlinelibrary.wiley.com/doi/pdf/10.1111/j.1502-3885.1997.tb00852.x.

Saatchi, Y., Turner, R., Rasmussen, C., 2010. Gaussian Process Change Point Models, pp. 927–934 (Haifa, Israel).

Sanjaume, E., Tolgensbakk, J., 2009. Beach ridges from the varanger peninsula (arctic Norwegian coast): characteristics and significance. Geomorphology 104 (1), 82–92.

Schanche, K., 1988. Mortensnes, en boplass i Varanger : en studie av samfunn og materiell kultur gjennom 10.000 år. Accepted: 2011-05-11T11:11:14Z Publisher:

Universitetet i Tromsø.

Schoonman, C., White, N., Pritchard, D., 2017. Radial viscous fingering of hot asthenosphere within the Icelandic plume beneath the North Atlantic Ocean. Earth Planet Sci. Lett. 468, 51–61.

Scott, D.B., Boyd, R., Medioli, F.S., 1987. Relative Sea-Level Changes in Atlantic Canada: Observed Level and Sedimentological Changes vs. Theoretical Models.

Shaochuan, L., 2021. Bayesian multiple changepoint detection for stochastic models in continuous time. Bayesian Analysis 16 (2), 521–544 (Publisher: International Society for Bayesian Analysis).

Shennan, I., 1986. Flandrian sea-level changes in the Fenland. I: the geographical setting and evidence of relative sea-level changes. J. Quat. Sci. 1 (2), 119–153. _eprint: https://onlinelibrary.wiley.com/doi/pdf/10.1002/jqs.3390010204.

Shennan, I., Horton, B., 2002. Holocene land- and sea-level changes in Great Britain. J. Quat. Sci. 17 (5–6), 511–526.

Shennan, I., Long, A.J., Horton, B.P., 2015. Handbook of Sea-Level Research. John Wiley & Sons (Google-Books-ID: ErbEBgAAQBAJ).

Shennan, I., Bradley, S.L., Edwards, R., 2018. relative sea-level changes and crustal movements in britain and Ireland since the last glacial maximum. Quat. Sci. Rev. 188, 143–159.

Shugar, D.H., Walker, I.J., Lian, O.B., Eamer, J.B.R., Neudorf, C., McLaren, D., Fedje, D., 2014. Post-glacial sea-level change along the Pacific coast of North America. Quat. Sci. Rev. 97, 170–192.

Sigmundsson, F., 1991. Post-glacial rebound and asthenosphere viscosity in Iceland. Geophys. Res. Lett. 18 (6), 1131–1134. _eprint: https://onlinelibrary.wiley.com/doi/pdf/10.1029/91GL01342.

Simkins, L.M., Simms, A.R., Dewitt, R., 2015. Assessing the link between coastal morphology, wave energy and sea ice throughout the Holocene from Antarctic raised beaches. J. Quat. Sci. 30 (4), 335–348. _eprint: https://onlinelibrary.wiley.com/doi/pdf/10.1002/jqs.2782.

Simonsen, A., 2005. Submerged Lacustrine Sediments and Sea-Level Fluctuations at Eigeroy, SW-Norway. Tech. Rep. Unpublished report, topo- graphical archive. Museum of Archaeology, Stavanger, Private Publisher, Stavanger.

Simpson, M., Breili, K., Kierulf, H.P., Lysaker, D., Ouassou, M., Haug, E., 2012. Estimates of Future Sea-Level Changes for Norway (Tech. rep., Kartverket, Norway).

Simpson, M., Nilsen, J.E., Ravndal, O., Breili, K., Sande, H., Kierulf, H., Steffen, H., Jansen, E., Carson, M., Vestøl, O., 2015. Sea Level Change for Norway: Past and Present Observations and Projections to 2100.

Sjöberg, L.E., Bagherbandi, M., 2020. Upper Mantle Density and Surface Gravity Change in Fennoscandia, p. 228428 determined from GRACE monthly data, Tectonophysics.

Smith, D.E., Harrison, S., Jordan, J.T., 2013. Sea level rise and submarine mass failures on open continental margins. Quat. Sci. Rev. 82, 93–103.

Snyder, J.A., Korsun, S.A., Forman, S.L., 1996. Postglacial emergence and the Tapes transgression, north-central Kola Peninsula, Russia. Boreas 25 (1), 47–56. _eprint: https://onlinelibrary.wiley.com/doi/pdf/10.1111/j.1502-3885.1996.tb00834.x.

Snyder, J.A., Forman, S.L., Mode, W.N., Tarasov, G.A., 1997. Postglacial relative sea-level history: sediment and diatom records of emerged coastal lakes, north-central Kola Peninsula, Russia. Boreas 26 (4), 329–346. _eprint: https://onlinelibrary.wiley.com/doi/pdf/10.1111/j.1502-3885.1997.tb00859.x.

Solem, J.O., Solem, T., Aagaard, K., Hanssen, O., 1997. Colonization and evolution of lakes on the central Norwegian coast following deglaciation and land uplift 9500 to 7800 years B.P. J. Paleolimnol. 18 (3), 269–281.

Solem, T., Solem, J.O., 1997. Shoreline displacement on the coast of Sor-Trondelag and More og Romsdal, Central Norway; a botanical and zoological approach. Nor. Geol. Tidsskr. 77 (3), 193–203. Place: Oslo Publisher: Scandinavian University Press WOS:A1997XU79000004.

Solheim, S., Persson, P., 2018. Early and mid-Holocene coastal settlement and demography in southeastern Norway: comparing distribution of radiocarbon dates and shoreline-dated sites, 8500–2000 cal. BCE. J. Archaeol. Sci.: Report 19, 334–343.

Sollid, J.L., Andersen, S., Hamre, N., Kjeldsen, O., Salvigsen, O., Sturød, S., Tveitå, T., Wilhelmsen, A., 1973. Deglaciation of Finnmark, north Norway. Norsk Geografisk Tidsskrift - Norwegian Journal of Geography 27 (4), 233–325. https://doi.org/10.1080/00291957308551960. Publisher: Routledge _eprint:

Sørensen, R., 1979. Late Weichselian deglaciation in the Oslofjord area, south Norway. Boreas 8 (2), 241–246. _eprint: https://onlinelibrary.wiley.com/doi/pdf/10.1111/j.1502-3885.1979.tb00806.x.

Sørensen, R., Henningsmoen, K., Høegh, H., Gälman, V., 2014. Holocene Land-hevningsstudier I Søndre Vestfold Og Sørsøstre Telemark—Revidert Kurve, *Vestfoldbaneprosjektet. Arkeologiske Undersøkelser I Forbindelse Med Ny Jernbane Mellom Larvik Og Porsgrunn Kommune. Bind 1. Tidlig- Og Mellommesolittiske Lokaliteter I Vestfold Og Telemark*, pp. 236–247.

Sørensen, T., 1985. Kystgeomorfologi På Lista, Vest-Agder Fylke. Master's thesis. University of Oslo.

St-Hilaire-Gravel, D., Bell, T.J., Forbes, D.L., 2010. Raised gravel beaches as proxy indicators of past sea-ice and wave conditions, lowther island, Canadian arctic archipelago. Arctic 63 (2), 213–226 (Publisher: Arctic Institute of North America).

Stabell, B., 1980. Holocene shorelevel displacement in Telemark, southern Norway. Nor. Geol. Tidsskr. 60 (7).

Stanford, J.D., Rohling, E.J., Hunter, S.E., Roberts, A.P., Rasmussen, S.O., Bard, E., McManus, J., Fairbanks, R.G., 2006. Timing of meltwater pulse 1a and climate responses to meltwater injections. Paleoceanography 21 (4). _eprint: https://onlinelibrary.wiley.com/doi/pdf/10.1029/2006PA001340.

Steffen, H., Kaufmann, G., 2005. Glacial isostatic adjustment of Scandinavia and northwestern Europe and the radial viscosity structure of the Earth's mantle. Geophys. J. Int. 163 (2), 801–812.

Steffen, H., Wu, P., 2011. Glacial isostatic adjustment in Fennoscandia—a review of data and modeling. J. Geodyn. 52 (3), 169–204.

Steffen, H., Wu, P., Wang, H., 2013. Optimal locations of sea-level indicators in glacial isostatic adjustment investigations. Solid Earth Discussions 5 (2), 2419–2448.

Steffen, H., Kaufmann, G., Lampe, R., 2014. Lithosphere and upper-mantle structure of the southern Baltic Sea estimated from modelling relative sea-level data with glacial isostatic adjustment. Solid Earth; Gottingen 5 (1), 447–459.

Steffen, R., Steffen, H., Weiss, R., Lecavalier, B.S., Milne, G.A., Woodroffe, S.A., Bennike, O., 2020. Early Holocene Greenland-ice mass loss likely triggered earthquakes and tsunami. Earth Planet Sci. Lett. 546, 116443.

Stokes, C.R., 2017. Deglaciation of the Laurentide ice sheet from the last glacial maximum. Cuadernos de Investigación Geográfica 43 (2), 377–428. Number: 2.

Stuiver, M., Polach, H.A., 1977. Discussion reporting of 14C data. Radiocarbon 19 (3), 355–363 (Publisher: Cambridge University Press).

Sutinen, R., Aro, I., Närhi, P., Piekkari, M., Middleton, M., 2014. Maskevarri Ráhppát in Finnmark, northern Norway – is it an earthquake-induced landform complex? Solid Earth **5** (2), 683–691. Publisher: Copernicus GmbH).

Sveian, H., Olsen, L., 1984. A shoreline displacement curve from Verdalsora, Nord-Trondelag, Central Norway. Nor. Geol. Tidsskr. 64 (1), 27–38. Publisher: Scandinavian University Press PO Box 2959 Toyen, Journal Division Customer.

Svendsen, J.I., Mangerud, J., 1987. Late Weichselian and holocene sea-level history for a cross-section of western Norway. J. Quat. Sci. 2 (2), 113–132.

Svendsen, J.I., Mangerud, J., 1990. Sea-level changes and pollen stratigraphy on the outer coast of Sunnmøre, western Norway. Nor. Geol. Tidsskr. 70 (2), 111–134.

Tanner, V., 1906. Studier ofver kvartarsystemet i Fennoskandias nordliga delar I. Fennia 23, 140.

Tarasov, L., Richard Peltier, W., 2002. Greenland glacial history and local geodynamic consequences. Geophys. J. Int. 150 (1), 198–229. _eprint: https://onlinelibrary.wiley.com/doi/pdf/10.1046/j.1365-246X.2002.01702.x.

Tarasov, L., Dyke, A.S., Neal, R.M., Peltier, W.R., 2012. A data-calibrated distribution of deglacial chronologies for the North American ice complex from glaciological modeling. Earth Planet Sci. Lett. 315–316, 30–40.

Thomas, M., Sündermann, J., 1999. Tides and tidal torques of the world ocean since the last glacial maximum. J. Geophys. Res.: Oceans 104 (C2), 3159–3183.

Thomsen, H., 1982. Late Weichselian shore-level displacement on Nord-Jæren, south-west Norway. Geol. Foren. Stockh. Forh. 103 (4), 447–468.

Thomsen, H., 1983. Sele-Rapporten. Resultatene fra den naturvitenskapelige forundersøkelsen fra Sele-Byberg området (Report from the Sele area. Preliminary studies based on natural sciences from the Sele-Byberg area)., Unpublished report. Museum of Archaeology, Stavanger, pp. 1–36.

Thomsen, H., 1989. Strandforskyvnings-undersøkelser i Kårstø-området : landskapsendringer gjennom de siste 13 000 år grunnet strandens skiftende beliggenhet. Tech. rep.. University of Stavanger, Stavanger. Arkeologisk museum i Stavanger, Accepted: 2017-07-20T13:02:02Z Publisher: Stavanger: Arkeologisk museum i Stavanger.

Tierney, J.E., Zhu, J., King, J., Malevich, S.B., Hakim, G.J., Poulsen, C.J., 2020. Glacial cooling and climate sensitivity revisited. Nature 584 (7822), 569–573. Number: 7822 Publisher: Nature Publishing Group.

Törnqvist, T.E., Rosenheim, B.E., Hu, P., Fernandez, A.B., 2015. Radiocarbon dating and calibration. In: Handbook of Sea-Level Research. John Wiley & Sons, Ltd,

pp. 347–360. Section: 23 _eprint: https://onlinelibrary.wiley.com/doi/pdf/10.1002/9781118452547.ch23.

Uehara, K., Scourse, J.D., Horsburgh, K.J., Lambeck, K., Purcell, A.P., 2006. Tidal evolution of the northwest European shelf seas from the Last Glacial Maximum to the present. J. Geophys. Res.: Oceans 111 (C9). _eprint: https://onlinelibrary.wiley.com/doi/pdf/10.1029/2006JC003531.

Ullman, D.J., Carlson, A.E., Hostetler, S.W., Clark, P.U., Cuzzone, J., Milne, G.A., Winsor, K., Caffee, M., 2016. Final Laurentide ice-sheet deglaciation and Holocene climate-sea level change. Quat. Sci. Rev. 152, 49–59.

Vacchi, M., Engelhart, S.E., Nikitina, D., Ashe, E.L., Peltier, W.R., Roy, K., Kopp, R.E., Horton, B.P., 2018. Postglacial relative sea-level histories along the eastern Canadian coastline. Quat. Sci. Rev. 201, 124–146.

van de Plassche, O., 1982. Sea-level Change and Water-Level Movements in the Netherlands during the Holocene. Ph. D. dissertation. Vrije Universiteit, Amsterdam.

Vasskog, K., Svendsen, J.-I., Mangerud, J., Haaga, K.A., Svean, A., Lunnan, E.M., 2019. Evidence of early deglaciation (18000 cal a bp) and a postglacial relative sea-level curve from southern Karmøy, south-west Norway. J. Quat. Sci. 34 (6), 410–423. _eprint: https://onlinelibrary.wiley.com/doi/pdf/10.1002/jqs.3109.

Vestøl, O., Ågren, J., Steffen, H., Kierulf, H., Tarasov, L., 2019. NKG2016LU: a new land uplift model for Fennoscandia and the Baltic Region. J. Geodes. 93 (9), 1759–1779.

Vetti, R.K.S., 2020. Isavsmelting Og Postglasiale Havnivåendringer Ved Nykvåg, Vesterålen. The University of Bergen. Accepted: 2020-06-16T04:31:44Z Publisher.

Virtanen, P., Gommers, R., Oliphant, T.E., Haberland, M., Reddy, T., Cournapeau, D., Burovski, E., Peterson, P., Weckesser, W., Bright, J., van der Walt, S.J., Brett, M., Wilson, J., Millman, K.J., Mayorov, N., Nelson, A.R.J., Jones, E., Kern, R., Larson, E., Carey, C.J., Polat, İ., Feng, Y., Moore, E.W., VanderPlas, J., Laxalde, D., Perktold, J., Cimrman, R., Henriksen, I., Quintero, E.A., Harris, C.R., Archibald, A.M., Ribeiro, A.H., Pedregosa, F., van Mulbregt, P., SciPy 1.0 Contributors, 2020. SciPy 1.0: fundamental algorithms for scientific computing in Python. Nat. Methods 17, 261–272.

Vorren, K.-D., 1978. Late and middle weichselian stratigraphy of andøya, north Norway. Boreas 7 (1), 19–38. _eprint: https://onlinelibrary.wiley.com/doi/pdf/10.1111/j.1502-3885.1978.tb00047.x.

Vorren, K.-D., Moe, D., 1986. The early Holocene climate and sea-level changes in Lofoten and Vester\aalen, North Norway. Nor. Geol. Tidsskr. 66 (2), 135–143.

Vorren, T.O., Vorren, K.-D., Alm, T., Gulliksen, S., Løvlie, R., 1988. The last deglaciation (20,000 to 11,000 B. P.) on Andoya, northern Norway. Boreas 17 (1), 41–77. _eprint: https://onlinelibrary.wiley.com/doi/pdf/10.1111/j.1502-3885.1988.tb00123.x.

Waelbroeck, C., Labeyrie, L., Michel, E., Duplessy, J.C., McManus, J.F., Lambeck, K., Balbon, E., Labracherie, M., 2002. Sea-level and deep water temperature changes derived from benthic foraminifera isotopic records. Quat. Sci. Rev. 21 (1), 295–305.

Whitehouse, P., Latychev, K., Milne, G.A., Mitrovica, J.X., Kendall, R., 2006. Impact of 3-D Earth structure on Fennoscandian glacial isostatic adjustment: implications for space-geodetic estimates of present-day crustal deformations. Geophys. Res. Lett. 33 (13).

Young, N.E., Briner, J.P., Miller, G.H., Lesnek, A.J., Crump, S.E., Thomas, E.K., Pendleton, S.L., Cuzzone, J., Lamp, J., Zimmerman, S., Caffee, M., Schaefer, J.M., 2020. Deglaciation of the Greenland and Laurentide ice sheets interrupted by glacier advance during abrupt coolings. Quat. Sci. Rev. 229, 106091.